Smoothed Particle Hydrodynamics simulations of reef surf zone processes driven by plunging irregular waves

Lowe, R. J.; Altomare, C.; Buckley, M. L.; da Silva, R. F.; Hansen, J. E.; Rijnsdorp, D. P.; Domínguez, J. M.; Crespo, A. J.C.

DOI
10.1016/j.ocemod.2022.101945

Publication date
2022

Document Version
Final published version

Published in
Ocean Modelling

Citation (APA)
Lowe, R. J., Altomare, C., Buckley, M. L., da Silva, R. F., Hansen, J. E., Rijnsdorp, D. P., Domínguez, J. M., & Crespo, A. J. C. (2022). Smoothed Particle Hydrodynamics simulations of reef surf zone processes driven by plunging irregular waves. *Ocean Modelling*, *171*, Article 101945. https://doi.org/10.1016/j.ocemod.2022.101945

Smoothed Particle Hydrodynamics simulations of reef surf zone processes driven by plunging irregular waves

Lowe, R. J.; Altomare, C.; Buckley, M. L.; da Silva, R. F.; Hansen, J. E.; Rijnsdorp, D. P.; Domínguez, J. M.; Crespo, A. J.C.

DOI
10.1016/j.ocemod.2022.101945

Publication date
2022

Document Version
Final published version

Published in
Ocean Modelling

Citation (APA)
Lowe, R. J., Altomare, C., Buckley, M. L., da Silva, R. F., Hansen, J. E., Rijnsdorp, D. P., Domínguez, J. M., & Crespo, A. J. C. (2022). Smoothed Particle Hydrodynamics simulations of reef surf zone processes driven by plunging irregular waves. *Ocean Modelling*, *171*, [101945]. https://doi.org/10.1016/j.ocemod.2022.101945

Ocean Modelling 171 (2022) 101945

Contents lists available at ScienceDirect

Ocean Modelling

journal homepage: www.elsevier.com/locate/ocemod

Smoothed Particle Hydrodynamics simulations of reef surf zone processes driven by plunging irregular waves

R.J. Lowe [a,b,c,*], C. Altomare [d], M.L. Buckley [e], R.F. da Silva [b], J.E. Hansen [b], D.P. Rijnsdorp [f], J.M. Domínguez [g], A.J.C. Crespo [g]

[a] Oceans Graduate School and UWA Oceans Institute, The University of Western Australia, Crawley, Australia
[b] School of Earth Sciences, The University of Western Australia, Crawley, Australia
[c] Australian Research Council Centre of Excellence for Coral Reef Studies, The University of Western Australia, Crawley, Australia
[d] Maritime Engineering Laboratory, Department of Civil and Environmental Engineering, Universitat Politecnica de Catalunya - BarcelonaTech (UPC), 08034 Barcelona, Spain
[e] U.S. Geological Survey, St. Petersburg Coastal and Marine Science Center, St. Petersburg, FL 33701, USA
[f] Environmental Fluid Mechanics Section, Faculty of Civil Engineering and Geosciences, Delft University of Technology, P.O. Box 5048, 2600 GA Delft, The Netherlands
[g] Environmental Physics Laboratory, CIM-UVIGO, Universidade de Vigo, Spain

ARTICLE INFO

Keywords:
Wave breaking
Surf zone
Wave runup
Wave modelling
Smoothed Particle Hydrodynamics
DualSPHysics

ABSTRACT

As waves interact with the slopes of coral reefs and other steep bathymetry profiles, plunging breaking usually occurs where the free surface overturns and violent water motion is triggered. Resolving these surf zone processes pose significant challenges for conventional mesh-based hydrodynamic models, due to the rapidly-deforming nature of the free surface and associated flows. Yet the accurate prediction of these surf zone hydrodynamics is critical for predicting a wide range of nearshore processes driven by wave breaking (e.g., wave dissipation and energy transfers; mean water levels and currents; and wave runup). In this study we assess the ability of the mesh-free, Lagrangian particle-based numerical modelling approach Smoothed Particle Hydrodynamics (SPH) based on DualSPHysics, to simulate the fine-scale hydrodynamic processes driven by irregular wave transformation over a fringing reef profile, by comparing results against detailed experimental observations from a physical modelling study. To greatly improve the computational efficiency, the SPH model was coupled to the mesh-based multi-layer nonhydrostatic wave-flow model SWASH. With this coupled approach, SWASH was used to efficiently simulate the evolution of non-breaking waves from the wavemaker up to the fore reef slope, with the SPH model then used to simulate the detailed hydrodynamic processes over the reef from just offshore of the breakpoint to the shoreline. The SPH model was able to accurately reproduce the complex free surface deformations during plunging breaking, the spectral evolution of waves across the reef flat (including nonlinear wave shape), the mean water levels and currents, and wave runup at the shoreline. Using the long duration simulations (>400 wave periods), the model was able to reproduce the full range of wave motions over the reef (from sea-swell to infragravity frequencies), including the increasing dominance of low frequency waves towards the shoreline and the large cross-reef standing wave motions excited by the reef geometry.

1. Introduction

Energy within wind-generated waves (periods 1–25 s) incident to coastlines drives a wide range of nearshore hydrodynamic processes that are responsible for wave-driven coastal flooding, sediment transport (including coastal erosion) and loads on coastal structures. While the processes governing wave transformation in the nearshore have been widely investigated for many decades, a complete understanding of the processes that control wave breaking in shallow water is still lacking, including knowledge of how wave energy is dissipated and converted into other forms of water motion. In the deep ocean where wind-generated waves occur over a wide range of frequencies, irregular waves propagate in groups, which transform as they enter shallow water. In the shoaling region and surf zone where rapid wave transformation occurs, organised wave motion initially evolves into highly nonlinear wave shapes, the free surface then overturns at the breakpoint, and water motions spanning a wide range of spatial and temporal scales are generated, ranging from small-scale (high frequency) turbulence to larger-scale (slowly-varying) currents and wave-driven mean water level variations (wave setup) (Svendsen, 2006). The time variation of breaking waves of different height generated by wave

* Correspondence to: The University of Western Australia, 35 Stirling Hwy, Crawley, Western Australia, Australia.
E-mail address: Ryan.Lowe@uwa.edu.au (R.J. Lowe).

https://doi.org/10.1016/j.ocemod.2022.101945
Received 4 August 2021; Received in revised form 4 December 2021; Accepted 8 January 2022
Available online 19 January 2022

groups also plays a critical role in nearshore hydrodynamics by generating low-frequency (infragravity) waves that can often be a dominant source of water motion near shorelines (Bertin et al., 2018). These low-frequency waves can also reflect from shorelines, creating cross-shore (partial-) standing waves that can become amplified by interactions with certain bathymetry profiles, such as reefs (e.g., Buckley et al., 2018; Péquignet et al., 2009; Gawehn et al., 2016; Becker et al., 2016).

Numerical wave models used to predict these nearshore hydrodynamics can be broadly classified as either phase-averaged or phase-resolving. Phase-averaged (or spectral) models attempt to simulate the properties of waves, usually based on linear wave theory (LWT), with empirical formulations to parameterise dissipation by wave breaking (e.g., Roelvink, 1993; Battjes, 1978; Thornton and Guza, 1983). Phase-resolving models aim to more directly simulate the nonlinear physics of individual waves, with Boussinesq (e.g., Shi et al., 2012; Madsen et al., 1997; Roeber et al., 2010) and nonhydrostatic wave models (e.g., Zijlema et al., 2011; Ma et al., 2012) being common examples. While these models can directly predict how non-breaking waves transform in the nearshore, including through nonlinear wave–wave interactions, Boussinesq and nonhydrostatic models do not capture all details of the wave breaking process, as they only provide a single-value representation of the free surface and hence cannot directly resolve the dynamics of overturning plunging waves that may influence how wave energy is dissipated (Blenkinsopp and Chaplin, 2007). While more computationally expensive than Boussinesq and nonhydrostatic models, phase-resolving Computational Fluid Dynamics (CFD) models attempt to more fully-resolve the vertical structure of breaking through numerical solution of the Navier–Stokes (N–S) equations. These CFD models can be broadly grouped into mesh-based and mesh-free models. Mesh-based models simulate Eulerian forms of the N–S equations on numerical grids (meshes). Mesh-free models solve Lagrangian forms of the N–S equations, which include those based on particle methods, such as SPH models, where the motion of a fluid continuum is described using discrete fluid 'particles'.

While mesh-based CFD models have been successfully applied in a number of surf zone studies (e.g., Jacobsen et al., 2012; Higuera et al., 2013; Chella et al., 2016; Mostert and Deike, 2020), they still face a primary challenge in how to accurately and efficiently resolve the complex, rapidly deforming free surfaces of breaking waves on fixed meshes. Numerical approaches have been developed to more accurately resolve the free surface, such as the Volume of Fluid (VOF) method (Hirt and Nichols, 1981) that has been most widely used in CFD applications of nearshore waves; however, these approaches can require high grid resolution at substantial computational expense to avoid significant errors in fluid properties near air–water interfaces, with development of optimal implementations still being an active area of research (Roenby et al., 2016). Lagrangian mesh-free particle-based models, such as Smoothed Particle Hydrodynamics (SPH) used in the present study, offer great appeal for simulating wave breaking, given that fluid at the free surface does not need to conform to a specified grid (Violeau, 2012). In addition, numerical implementations of particle-based models (i.e., based on SPH) using weakly-compressible flow theory are ideally suited for massive parallelisation (e.g., on Graphics Processor Units, GPUs) (e.g., Domínguez et al., 2013), allowing for larger-scale CFD simulations to be conducted much more efficiently. Nevertheless, despite many advances occurring over the past decade, SPH models also face a number challenges that are often distinct from mesh-based models, which have motivated considerable research over the past decade (e.g., Gotoh and Khayyer, 2018; Violeau and Rogers, 2016; Vacondio et al., 2021).

Since early applications of SPH models to study breaking waves (Dalrymple and Rogers, 2006; Lo and Shao, 2002), SPH applications to nearshore hydrodynamic problems have greatly accelerated over the past decade (see (Gotoh and Khayyer, 2018) for a review). Initially, computational limitations restricted these nearshore wave applications of SPH models to relatively small domains and/or using coarse resolution with simulations of relatively short duration (just like mesh-based CFD model counterparts); hence, focusing on regular or solitary waves that could be conducted within order 10s of wave periods (e.g., Dalrymple and Rogers, 2006; Lo and Shao, 2002; Gotoh et al., 2004). With advances in computational performance, larger-scale and/or longer duration applications of CFD models (both mesh-based and mesh-free) are becoming increasingly possible, including simulations of more realistic irregular wave conditions that require simulating of order 100 wave periods or longer. The ability to simulate irregular waves is often important to provide a more complete description of nearshore hydrodynamics, as breaking wave groups generate infragravity waves that often become a dominant source of water motion near shorelines. Some CFD modelling studies have successfully simulated infragravity wave dynamics generated by irregular waves over sandy beaches and armoured foreshores (e.g., Torres-Freyermuth et al., 2010; Wen and Ren, 2018), which have tended to resolve approximately 100 wave periods that is sufficient to simulate higher frequency infragravity motions at wave group time-scales. However, for other nearshore systems, much longer period infragravity motions can often be dominant, especially when these waves interact with larger-scale bathymetric features such as reefs (e.g., Buckley et al., 2018; Gawehn et al., 2016; Becker et al., 2016).

In this study, we applied the SPH approach using DualSPHysics (Domínguez et al., 2021) to conduct highly-resolved numerical simulations of irregular wave transformation over a fringing reef profile, to investigate the capability of the model to predict the broad range of hydrodynamic processes that contribute to water level variability across the reef, including the nonlinear evolution and dissipation of sea-swell waves, the generation and propagation of infragravity waves, wave setup and mean currents, and wave runup at the shoreline. The model was validated using detailed measurements of waves, velocities, mean water levels and wave runup from a physical modelling study of a 1:36 scaled fringing reef profile with a steep fore reef slope and wide reef flat, conducted in a 55-m-long wave flume by Buckley et al. (2015) (Fig. 1). In order to greatly boost computational efficiency, the DualSPHysics model was coupled to the phase-resolving nonhydrostatic wave-flow model SWASH (Zijlema et al., 2011) that simulated waves in the region offshore of the reef; thus concentrating the SPH simulations in shallow water where wave transformation occurs over the reef profile. Using this coupled modelling approach, long duration simulations were achieved (duration >400 peak wave periods or equivalent to >90 min in field time-scales), which enabled the low-frequency motions that make the dominant swash contribution to runup to be accurately resolved. Overall, the results from these simulations provide an unprecedented view of the wave transformation within a reef surf zone at fine-resolution, providing new insight into the range of wave-driven reef hydrodynamic processes that are responsible for wave runup at reef coastlines.

2. Model description

2.1. The SPH approach

The numerical simulations were conducted using the Lagrangian mesh-free SPH approach, where a fluid continuum is discretised into 'particles' that represent computational nodal points where mass and momentum conservation laws (N–S equations) are solved (Monaghan, 1992). The kinematic and dynamic properties of each particle (i.e., position, density, pressure, and velocity) are then determined by interpolation of the properties of neighbouring particles using a weighted kernel function (W) applied over a characteristic smoothing length (h_{SPH}). Therefore, in the SPH approach any function $F(\vec{r})$ in coordinate space $\vec{r}$ is mathematically defined by the integral expression

$$F(\vec{r}) = \int F(\vec{r}')\, W(\vec{r} - \vec{r}', h_{SPH})\, d\vec{r}' \tag{1}$$

This function F can be discretised based on particles, where the approximation of the function is interpolated at particle i and the

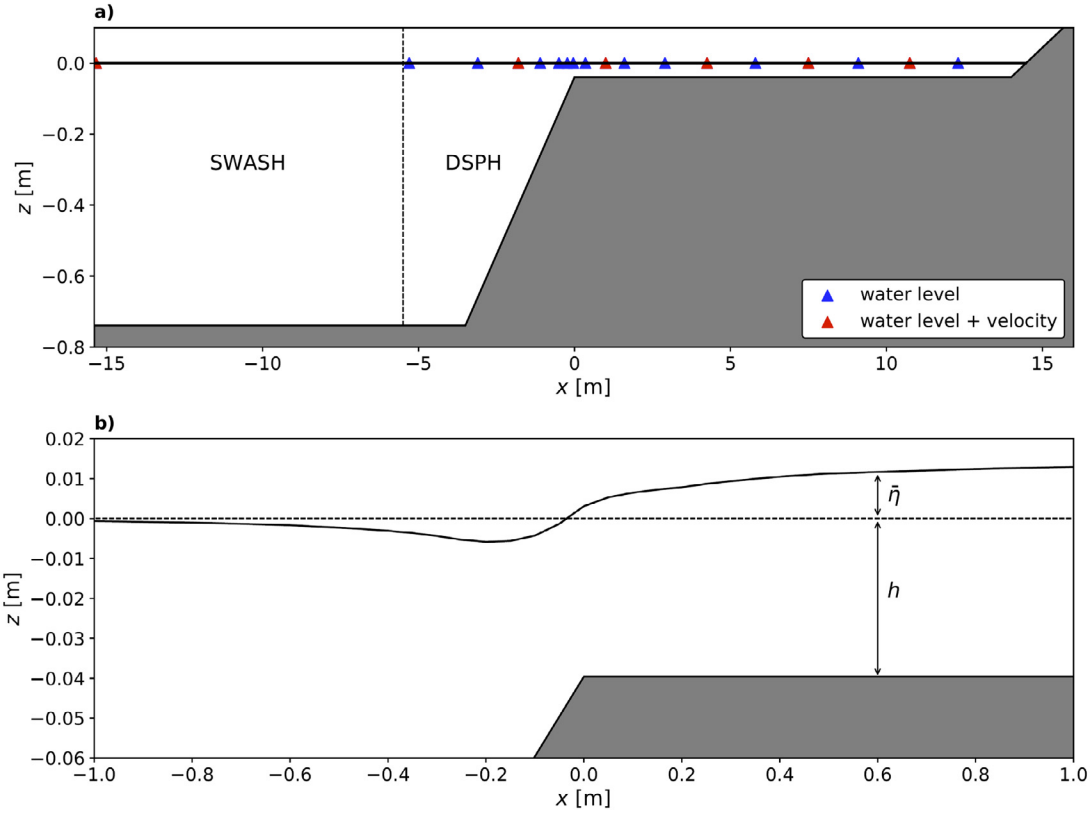

Fig. 1. (a) Experimental setup in Buckley et al. (2015) denoting locations of water level measurements (blue triangles) and locations with water level and velocity measurements (red triangles). The solid horizontal line at $z = 0$ m denotes the still water level. The vertical dashed line represents the SWASH coupling location with DualSPHysics. Note that the SWASH offshore boundary is located at the offshore wave gauge at $x = -15.34$ m, with the wavemaker located further offshore at $x = -31$ m (not shown). (b) Wave setup profile ($\bar{\eta}$) (solid line) and still water depth (h) relative to the still water level (dashed line). Note that the vertical scale of the axis in (b) has been exaggerated in both figures.

summation is performed over all the particles j that are located within the kernel region:

$$F\left(\vec{r}_i\right) \approx \sum_j F\left(\vec{r}_j\right) W\left(\vec{r}_{ij}, h_{SPH}\right) V_j \tag{2}$$

where $V_j = m_j/\rho_j$ is the volume associated with a neighbouring particle j, $\vec{r}_{ij} = \vec{r}_i - \vec{r}_j$ is the distance between particle i and j, and m and ρ are mass and density, respectively. To achieve a sufficient number of particle interactions within the kernel while still constraining the number of neighbour particle interactions requiring computation, the kernel function in Eq. (2) is implemented with a finite distance cut-off. Note that in this study we use a quintic kernel where particle interactions at distances $>2h_{SPH}$ are neglected (Wendland, 1995).

In this study, the N–S equations are solved using the Weakly Compressible SPH (WCSPH) approach, where following Monaghan (1994), pressure (P) is efficiently obtained through its relation to density by solving an equation of state in the form (Batchelor, 1974)

$$P = B\left[\left(\frac{\rho}{\rho_0}\right)^{\gamma} - 1\right] \tag{3}$$

where $\gamma = 7$ is the polytropic constant and $B = c_0^2\rho_0/\gamma$ is defined based on the reference density $\rho_0 = 1000$ kg m^{-3} and c_0 is the speed of sound at the reference density. The ability to solve for pressure using Eq. (3) in an explicit form greatly reduces computational times and can also be more readily parallelised in numerical codes, and is thus well-suited for solution on GPUs (see below). However, the main drawback of WCSPH is the potential for noise in the pressure / density fields, which is often mitigated by employing a range of density diffusion approaches (Molteni and Colagrossi, 2009), with use of the δ-SPH formulation being common (Antuono et al., 2012). In the present study we use a new density diffusion term based on Fourtakas et al. (2019) that is less dissipative compared to the standard δ-SPH approach, which as we show below, offers improvements in the prediction of wave propagation over long distances.

Within the WCSPH approach, conservation of mass is expressed as

$$\frac{d\rho_i}{dt} = \sum_j m_j \vec{u}_{ij} \cdot \nabla_i W_{ij} + \delta h_{SPH} c_0 \sum_j \psi_{ij} \cdot \nabla_i W_{ij} V_j \tag{4}$$

where $\vec{u}_{ij} = \vec{u}_i - \vec{u}_j$ with $\vec{u}_i = d\vec{r}_i/dt$ representing the velocity of particle i, and the last term in Eq. (4) is a diffusion term based on Fourtakas et al. (2019). Here $\delta = 0.1$ is a specified coefficient and ψ_{ij} is a density diffusion term (see Section 2.2). Similarly, conservation of momentum can be expressed as (Monaghan, 1992)

$$\frac{d\vec{u}_i}{dt} = -\sum_j m_j \left(\frac{P_i + P_j}{\rho_i \rho_j}\right) \nabla_i W_{ij} + \vec{g} + \Gamma_i \tag{5}$$

where $\vec{g}$ is gravitational acceleration and Γ is a viscous dissipation (stress) term. The viscous dissipation term is commonly described using an artificial viscosity approach (Monaghan, 1992), but also variants based on turbulence closure models (reviewed in (Gotoh and Khayyer, 2018)) (see Section 2.2).

2.2. The DualSPHysics model

In this study, we applied version 5.0 of the open-source SPH model DualSPHysics (http://dual.sphysics.org/) that solves the N–S equations (Eqs. (4) and (5)) using the parallel computing power of either CPUs and/or GPUs (Crespo et al., 2015; Domínguez et al., 2021). The present model configuration and settings are generally similar to the study by Lowe et al. (2019) (based on version 4.2), but include some improvements using new features in version 5.0 that are detailed below. At the solid boundaries, we applied a new modified Dynamic Boundary Condition (mDBC) approach based on English et al. (2021). This

mDBC approach overcomes some of the drawbacks of the original Dynamic Boundary Condition (DBC) approach in DualSPHysics (Crespo et al., 2007), resulting in less dissipation in flows near boundaries and reducing unphysical pressure / density values for the boundary and adjacent fluid particles. The mDBC approach employs ghost nodes using an extrapolation method similar to the one proposed in Tafuni et al. (2018) to calculate the properties of boundary particles, requiring a layer consisting of several boundary particles to be included to avoid kernel truncation errors for fluid particles near the boundaries (a layer of five boundary particles was used in this study, which covers the distance of interaction defined by the kernel radius of $2h_{SPH}$). While the mDBC can use the same boundary particle arrangement of the original DBC, it defines the boundary interface at half the inter-particle spacing (dp) from the inner most layer of boundary particles. Hence, when simulating a physical model test, the boundary interface must correspond to the physical boundary, while the inner most layer of boundary particle is created at a distance equal to $dp/2$.

In Lowe et al. (2019), the viscous dissipation term (Γ_i) in Eq. (5) was modelled based on the widely used artificial viscosity approach that is linearly proportional to local velocity gradients and parameterises the effect of a shear and bulk viscosity. While the artificial viscosity approach is widely used in wave breaking applications (De Padova et al., 2014), the scheme can be overly dissipative by generating excess shear forces (Taylor and Miller, 2012), which may affect coherent turbulent flow structures under breaking waves (Dalrymple and Rogers, 2006). Therefore, in the present study we also assessed the use of a Laminar viscosity plus Sub-Particle Scale (SPS) turbulence closure model (Gotoh et al., 2004; Dalrymple and Rogers, 2006) based on the Large Eddy Simulation (LES) approach (Smagorinsky, 1963), analogous to Sub-Grid Scale (SGS) models used in turbulent incompressible flow simulations on fixed meshes. For this approach, the viscous dissipation term is expressed as

$$\Gamma_i = \underbrace{\sum_j m_j \left(\frac{4\nu_0 \vec{r}_{ij} \cdot \nabla_i W_{ij}}{\left(\rho_i + \rho_j\right)\left(r_{ij}^2 + \varepsilon^2\right)} \right) \vec{u}_{ij}}_{\text{Laminar}} + \underbrace{\sum_j m_j \left(\frac{\vec{\tau}_{ij}^{\,i}}{\rho_i^2} + \frac{\vec{\tau}_{ij}^{\,j}}{\rho_j^2} \right) \nabla_i W_{ij}}_{\text{Sub-Particle Scale turbulence}}, \tag{6}$$

where the first term describes the effect of laminar viscous stresses and second term represents the SPS turbulent stresses. Here ν_0 is the kinematic viscosity, $\varepsilon^2 = 0.01h_{SPH}^2$, and $\vec{\tau}_{ij}$ is the SPS stress tensor. The SPS stress tensor is defined as (Dalrymple and Rogers, 2006) based on a Smagorinsky model (Smagorinsky, 1963)

$$\frac{\vec{\tau}_{ij}}{\rho} = \nu_t \left(2s_{ij} - \frac{2}{3} k \delta_{ij} \right) - \frac{2}{3} C_I \Delta^2 \delta_{ij} \left| s_{ij} \right|^2, \tag{7}$$

where k is the SPS turbulent kinetic energy, s_{ij} is the strain tensor, Δ is the initial inter-particle spacing, and $C_I = 0.0066$ is an empirical parameter. The turbulent eddy viscosity (ν_t) is defined as $\nu_t = \left(C_s \Delta\right)^2 \sqrt{2 s_{ij} s_{ij}}$, where $C_s = 0.12$ is the Smagorinsky constant.

2.3. SWASH coupling

DualSPHysics can generate waves using several different approaches. In Lowe et al. (2019), moving boundary particles were used to simulate the movement of a piston wavemaker in a physical modelling study (Altomare et al., 2017), which generated regular waves across two bathymetry profiles: a plane beach (Ting and Kirby, 1996), (Ting, 1995) and a fringing reef (Yao et al., 2012). In that study, Lowe et al. (2019) was able to substantially shorten the deep and flat offshore region in the flumes. This greatly reduced computational times, enabling an order 100 waves to be simulated, while having negligible influence on the results.

Due to the irregular wave conditions in the present study, which required resolving the evolution of dispersing waves down the flume from the physical wave maker and simulating several hundred waves to achieve statistical convergence, wave generation posed several challenges that required adopting new approaches. Thus, in this present study the DualSPHysics model was coupled to the nonhydrostatic wave-flow model SWASH (Zijlema et al., 2011) using a recently developed open-boundary condition approach (inlet/outlet) that passes flow properties from SWASH to DualSPHysics (Verbrugghe et al., 2019b). In DualSPHysics, the open boundaries consist of a buffer zone (width of 8 layers of particles). When open boundaries are employed in coupled model applications, physical quantities such as velocity, pressure and surface elevation are imposed in the buffer zone. The coupling uses a one-way offline scheme, with the SWASH model executed beforehand to provide the velocity and water surface elevation information at the coupling point location. With SWASH run in multi-layered mode, velocities are interpolated between each SWASH layer and assigned to the SPH particles within the buffer zone via postprocessing. To avoid unwanted reflection at offshore inlet/outlet boundary, reflection compensation is also applied to correct the velocity and surface elevation imposed in the inlet zone. The correction uses the measured free surface close to the buffer interface and linear long-crested wave theory in shallow water to specify the reflection compensation (Verbrugghe et al., 2019a; Altomare et al., 2017).

3. Case study

3.1. Experimental data (Buckley et al., 2015)

This study numerically simulates experimental results from Buckley et al. (2015), which measured wave transformation, wave setup and wave runup across a scaled physical model of a fringing reef in a 55-m long wave flume (Fig. 1a). The bathymetry profile, constructed from smooth marine plywood, had a steep (1:5) fore reef slope, a 14 m wide reef flat, and a 1:12 sloping beach. At the 1:36 geometric scaling used in the experiments, the width of the reef flat is equivalent to 500 m at field scale, which is typical of global averages (Falter et al., 2013). Irregular waves with a TMA-type spectrum were generated 31 m seaward of the reef crest (with the crest defined as $x = 0$ m) by a piston-type wave maker with second-order wave generation and active reflection compensation. In the experiments, a wide range of incident wave conditions and offshore water levels were considered (16 runs in total, Table 2 of (Buckley et al., 2015)). Due to the computational demand of the numerical simulations, the present study focuses on investigating one of these experimental cases in detail (Run 2), which used a still water depth over the reef flat of $h_r = 0.04$ m (equivalent to 1.4 m in field scale). The wavemaker generated spectral waves with a root-mean-squared wave height of $H_{rms,0} = 0.06$ m (2.2 m in field scale) and a peak period $T_p = 2.26$ s (13.6 s in field scale). This set of wave and water level conditions was intermediate (and considered most representative) of the broader range of conditions reported in the Buckley et al. (2015) experiment.

The experiment lasted 41 min, during which time and water levels were measured at 18 locations along the flume with resistance-type wave gauges, and horizontal velocities were measured at 6 locations with electromagnetic current metres (ECM), with all instruments sampling synchronously at 40 Hz (Fig. 1a). In addition, georeferenced video imagery (2448 × 800 pixel resolution) of the reef crest region from $x = -1$ m to 1 m (pixel resolution ~1 mm) was recorded at 25 Hz. Images in pixel coordinates were converted to real-world coordinates using six control points placed on the front glass of the flume and the methods outlined in Bruder and Brodie (2020). With this calibration, the average horizontal and vertical root-mean-squared reprojection error was 1.2 mm.

3.2. Model configuration and numerical simulations

The numerical simulations were conducted in a 2DV (vertical) plane. The model domain extended from just seaward of the toe of the fore reef slope ($x = -5.5$ m), coinciding with the SWASH coupling point (see below), to $x = +20$ m (Fig. 1a). For the simulations, an initial inter-particle spacing of $dp = 3$ mm was used, with smaller values of dp having a negligible influence on the results (see Appendix A.1). This translated into ~450,000 particles being simulated, which varied on a wave-by-wave basis due to the inlet–outlet boundary conditions. The characteristic smoothing length (h_{SPH}) used for the kernel averaging (Eq. (2)) is related to the initial inter-particle spacing according to $h_{SPH} = coefh\sqrt{2}dp$, where $coefh$ is a coefficient of order 1 that determines the spatial-scale of interactions with surrounding particles. If the value of $coefh$ is too low, this can lead to greater numerical dissipation (e.g., wave attenuation when simulating relatively long wave flumes; Roselli et al. (2018)) due to weaker interactions with neighbouring particles; however, larger values of $coefh$ reduce the effective model resolution. In the present study, a value of $coefh$=1.5 was used, which fell within the range (1.2–1.8) that Lowe et al. (2019) found had minimal effect on wave transformation; this was confirmed with initial testing with values of $coefh$ between 1.4 and 1.8 having negligible influence on the results (see Table A.1 in Appendix A.1).

To model viscous dissipation, both the artificial viscosity and Laminar + SPS turbulence modelling approach (Eq. (6)) were considered in initial testing (see Appendix A.1 for a comparison of results with both approaches). We note that for 2DV simulations, the LES-based SPS approach would only describe the 2D features of surf zone eddies and thus cannot resolve the small-scale 3D turbulent flow structures that are required to properly resolve the turbulent energy cascade from large- to small-scale eddies where turbulent kinetic energy is dissipated. Nevertheless, a number of 2D SPH studies have found that use of an SPS closure model can give robust results of surf zone hydrodynamics (e.g., Dalrymple and Rogers, 2006; Gotoh et al., 2004; Makris et al., 2016; Shao and Ji, 2006). In Appendix A.1, we found some slight improvement in wave transformation using the Laminar + SPS approach compared to using artificial viscosity, with less dissipation occurring within the inner surf zone following initial breaking, which more closely matched the experiments. Therefore, all results presented below are based on results using the Laminar + SPS approach, using a kinematic viscosity for water of $\nu_0 = 1 \times 10^{-6}$ m^2 s and default parameters within the Smagorinsky turbulence model (Eq. (7)).

The DualSPHysics model was one-way coupled to a larger SWASH model domain that extended to the offshore combined wave and velocity measurement location at $x = -15.3$ m to $x = +20$ m (Fig. 1a). The SWASH model was run in multi-layer (2DV) mode using a uniform horizontal resolution of 0.05 m and using 10 vertical sigma layers. At the offshore open boundary, a weakly reflective boundary condition was applied driven by Fourier series coefficients (amplitude, frequency and phase) that enabled arbitrary incident wave timeseries to be generated. These Fourier coefficients were derived from the incoming (shoreward) component of the water level timeseries from the offshore wave and velocity measurements at $x = -15.3$ m, with frequencies less than 1/2 the peak wave frequency removed to force the model with only incident SS waves. Following Buckley et al. (2015), the incoming water level signal was derived from the synchronised water level and velocity timeseries using a frequency domain algorithm. In this approach, Fourier components of the water level and velocity spectra were applied with linear wave theory to compute directionally-separated (incoming and outgoing) wave spectra, with inverse Fourier transformations used to generate timeseries of incoming- and outgoing-propagating wave signals (refer to Appendix B in Buckley et al. (2015) for details). Water levels and layer velocities output by SWASH at the $x = -5.5$ m coupling location were converted offline to the inlet–outlet boundary conditions (water levels and velocities interpolated to particle locations) to force DualSPHysics.

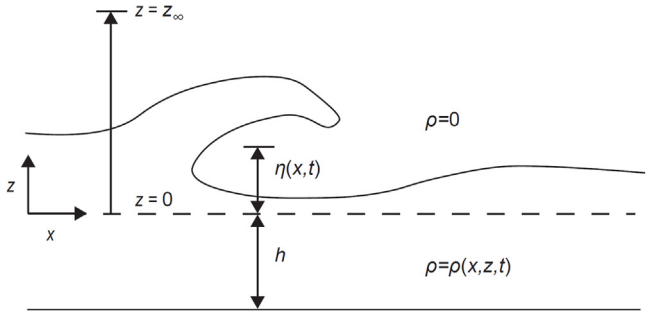

Fig. 2. Definitions of the still water depth (h) and surface elevation (η) defined based on integrating the variable density field $\rho(x, z, t)$ using Eq. (8) from the bottom ($z = -h$) to a constant reference elevation ($z = z_\infty$) that is always above water.

The SWASH and DualSPHysics models were run for a period commencing 10 min (600 s) into the experiment for a duration of 16 min (960 s), with output for both models stored at 20 Hz. Based on the peak period ($T_p = 2.26$ s), this duration equates to 425 waves, which was found to be adequate for the statistics of the full range of hydrodynamic processes to converge (i.e., *SS* waves, *IG* waves and wave setup) (see Appendix A.1). The numerical simulations were conducted at the Pawsey Supercomputing Centre in Perth, Australia on its Nimbus cloud computing infrastructure, using a GPU-enabled compute node housing an Intel Xeon Silver 4215 2.50 GHz Processor (8 core, 16 thread), 45 GB RAM, and a Nvidia Tesla V100 GPU (5120 CUDA cores). DualSPHysics took 107 hr to simulate the 960 s experimental period using ~450,000 particles, with the SWASH model and wave boundary condition generation taking 24 min.

3.3. Post-processing and data analysis

To visualise features of the simulated breaking waves and relate these to the experimental georeferenced video imagery, the air–water interface was identified from the raw simulated particle data output by computing isosurfaces using the marching cubes algorithm (Lorensen and Cline, 1987). For quantitative comparison of the simulated water levels with the wave gauge data, the densities of the particles were postprocessed to fixed grids (resolution varying depending on application) by interpolating onto the grid using a Wendland kernel function with averaging length $2h_{SPH}$ (see Section 2.1). Post-processing of the model output was used to compute surface elevations at a horizontal resolution $\Delta x = 5$ cm. We note that for cases where the free surface overturned there can be multiple air–water interfaces and hence multiple definitions of the "free surface" (Lowe et al., 2019), and that it is also unclear what water level a resistance wire wave gauge would exactly record when there is a mixture of water and air along the gauge within the surf zone (Stive and Wind, 1982). In this study we define the free surface elevation (η) by the vertical mass-weighted average water level (Fig. 2):

$$\eta = \frac{1}{\rho_0}\int_{-h}^{z_\infty} \rho dz - h, \tag{8}$$

which was obtained by vertically-integrating the mass in the water column at $\Delta z = 1$ mm vertical resolution, from the bottom ($z = -h$) (where h represents the still water depth, Fig. 1b) to the top of the interpolation grid (denoted $z = z_\infty$), with the elevation z_∞ chosen to ensure the upper integration limit never contained water (where, by definition, $\rho = 0$ kg m^{-3} for void regions that do not contain water). Other gridded model output (i.e., density, pressure and velocity components) were interpolated using the same Wendland kernel function, with different resolution chosen for different applications: (1) a grid with resolution $\Delta x = 5$ cm and $\Delta z = 5$ mm extending over the full model domain, and (2) a finer grid focused on the surf zone ($x = -2.0$ m to $+4.0$ m) with resolution $\Delta x = 6$ mm and $\Delta z = 3$ mm. To calculate wave runup, a

numerical water level gauge was implemented along the 1:12 beach slope at a height 3 mm above the bed (equivalent to one dp, the initial inter-particle distance), which searched for the runup elevation every 1 mm along the slope.

The results were analysed over the final 900 s of the DualSPHysics simulations, thus ignoring the initial 60 s of the simulation to allow time for the model results to spin up. Wave setup $\overline{\eta}$ was calculated from the time-averaged water level relative to still water level by removing an offshore mean reference level defined by the spatial-average between $x = -4.0$ m to -2.0 m, where wave setup/setdown was negligible and the overbar denotes time averaging. The wave component of water level variability ($\widetilde{\eta} = \eta - \overline{\eta}$) was used to compute wave spectra $P_{\eta\eta}(f)$ by applying Welch's method using a Hanning window with 50% overlap and a segment length of 2^{12} samples (205 s, equivalent to ~20 min in field scale). Following Buckley et al. (2018), the spectra were separated into sea-swell (*SS*, $f \geq 0.22$ Hz) and infragravity (*IG*, $f < 0.22$ Hz) frequency bands, where 0.22 Hz corresponds to one-half of the peak frequency of the incident wave spectrum (equivalent to a 27 s wave period in field scale). The infragravity frequency band was further separated into high infragravity (*IG-H*, 0.22 Hz > $f \geq$0.06 Hz) and low infragravity (*IG-L*, $f < 0.06$ Hz) contributions, with the separation frequency equivalent to 100 s in field scale.

Root-mean-squared wave heights H_{rms} for each frequency band were calculated as $H_{rms} = \sqrt{8m_0}$, where $m_0 = \int_{f_{low}}^{f_{high}} P_{\eta\eta}(f)\,df$ is the zeroth spectral moment integrated over a range from f_{low} to f_{high} based on the defined limits of each frequency band (*SS*, IG_H, and IG_L). Other bulk wave parameters evaluated include the spectral period ($T_{m-1,0}$), a characteristic wave period that is commonly related to wave runup and overtopping predictions (Hofland et al., 2017), which is defined as $T_{m-1,0} = m_{-1}/m_0$, where the nth spectral moment is $m_n = \int_0^\infty f^n P_{\eta\eta}(f)\,df$; as well as the spectral width (ν) that measures how broadly distributed wave energy is across frequencies, which is defined as $\nu = \sqrt{m_0 m_2/m_1^2 - 1}$. To evaluate the cross-shore evolution in the nonlinearity of wave shape, the skewness (*Sk*) and asymmetry (*As*) were calculated from the wave ($\widetilde{\eta}$) timeseries as (e.g., Ruessink et al., 2012):

$$Sk = \frac{\overline{\widetilde{\eta}^3}}{\left(\overline{\widetilde{\eta}^2}\right)^{3/2}}, \quad As = \frac{\overline{\widetilde{\eta}_H^3}}{\left(\overline{\widetilde{\eta}^2}\right)^{3/2}} \tag{9}$$

where $\widetilde{\eta}_H$ denotes the Hilbert transform of $\widetilde{\eta}$. Skewness describes how much more the crest is elevated and narrower relative to the trough, while asymmetry describes how pitched forward/backward (i.e., "saw-toothed") the waves are. The skewness and asymmetry of the wave velocities across the reef were also investigated, by replacing water level with velocity in Eq. (9).

To investigate the generation and propagation of IG waves over the reef, the relationship between the incident SS wave groups and IG waves were evaluated in the time-domain by first filtering the water level timeseries into SS ($\widetilde{\eta}_{SS}$) and IG ($\widetilde{\eta}_{IG}$) wave components using a fifth-order Butterworth filter with a frequency cut-off of $f = 0.22$ Hz. Using the SS water level timeseries at the offshore gauge location at $x = -15.34$ m, where synchronised wave and velocity timeseries were recorded (Fig. 1a), a Hilbert transform was applied to the incoming component of the water level timeseries obtained by directional separation (see Section 3.2) to obtain the incoming SS wave envelope offshore $SS_{env,0}$. By comparing lagged cross-correlations between $SS_{env,0}$ and the IG water level timeseries across the reef, characteristic features of the IG wave generation and propagation (including reflection) were compared between the model predictions and observations (e.g., Janssen et al., 2003).

Wave runup timeseries were used to compute the significant wave runup (R_{sig}) defined as

$$R_{sig} = R_{setup} + R_{swash} \tag{10}$$

where R_{setup} is the steady mean runup elevation relative to the offshore mean water level (i.e., wave setup at the shoreline) and $R_{swash} = S_{sig}/2$ is the swash contribution related to one-half of the significant swash excursion S_{sig}. The significant swash excursion was evaluated from the wave runup spectra as $S_{sig} = 4\sqrt{m_0}$, where here m_0 is the zeroth spectral moment of the runup spectra. Similar to the approach used for wave heights, the swash contribution to wave runup (R_{swash}) was decomposed into sea-swell, high infragravity and low infragravity contributions, denoted $R_{swash,SS}$, $R_{swash,IG-H}$ and $R_{swash,IG-L}$, respectively.

4. Results

4.1. Wave transformation and runup

An illustrative example of a single breaking wave sequence simulated by the model is shown in Fig. 3, where the internal flow structure is visualised with colours representing the horizontal (u) component of velocity at the individual particle locations. As the wave approaches the reef, it becomes asymmetric with a near-vertical face (Fig. 3a). The crest of the wave then overturns as a plunging jet (Fig. 3b), hitting a thin layer of water retreating down the fore reef slope, which causes a splash-up of the free surface (Fig. 3c). The volume of water in the breaking wave moves shoreward over a seaward-directed bottom flow, which oscillates vertically across the reef flat and generates a trail of surf zone eddies (localised areas of negative velocities below positive velocities) in the vertical plane (Fig. 3d–g). The wave then develops into a more organised bore-like feature that propagates shoreward across the reef flat (Fig. 3 h–j).

For comparison with the experimental observations, this same breaking wave sequence is compared against georeferenced video imagery (Fig. 4), with isosurfaces computed from the synchronised model predictions superimposed as red lines. The SPH model generally reproduces this free surface evolution well, capturing the plunging jet, the characteristics of the wave splash-up, and the propagation of a bore-like feature across the reef flat. For a longer 30 s sequence of the video record capturing 13 waves, a time sequence of vertical columns of pixels are shown at two locations ($x = -0.23$ m and $x = +0.35$ just seaward and shoreward of the reef crest, respectively) (Fig. 4k–l). The superimposed free surface elevation timeseries agrees well with the video observations at both locations, capturing the skewed and asymmetric shapes of the individual waves.

Predictions of the transformation of individual waves (height, shape and phase) across the reef also agree well with the full set of wave gauge measurements (Fig. 5). The model captures the change in wave shape as they shoal on the fore reef slope. Near the crest where waves break (i.e., gauges 7–9, Fig. 5), the height of the waves rapidly decreases, and saw-toothed bores emerge that are reproduced by the model. As the back of the reef flat is approached, the heights of the sea-swell waves decrease appreciably. Within this back-reef region, individual waves tend to be associated with high frequency oscillations in the free surface, which are present both in the observations and model predictions. These high frequency oscillations are features of undular bores that are commonly observed during wave transformation over coral reef flats (Sous et al., 2019; Tissier et al., 2018).

The predicted sea-swell wave heights ($H_{rms,SS}$) closely follow the observations, with $H_{rms,SS}$ initially shoaling on the fore reef, rapidly decreasing after the breakpoint at $x_b \approx -0.2$ (just seaward of the crest), and then becoming nearly constant at $H_{rms,SS} \approx 1$ cm for $x \gtrsim 1$m (albeit still decaying towards shore at a low rate) (Fig. 6a). There is only some discrepancy at the wave gauge at x=-0.2 m (located immediately at the break point), where the observed $H_{rms,SS}$ is higher. This gauge corresponds with the typical location of the overturning free surface during breaking (Fig. 4), where the free surface takes multiple values and there would be significant entrainment of air; both of which would likely add uncertainty to measurements at this location. The height of the high frequency component of the IG waves ($H_{rms,IG-H}$) is also very

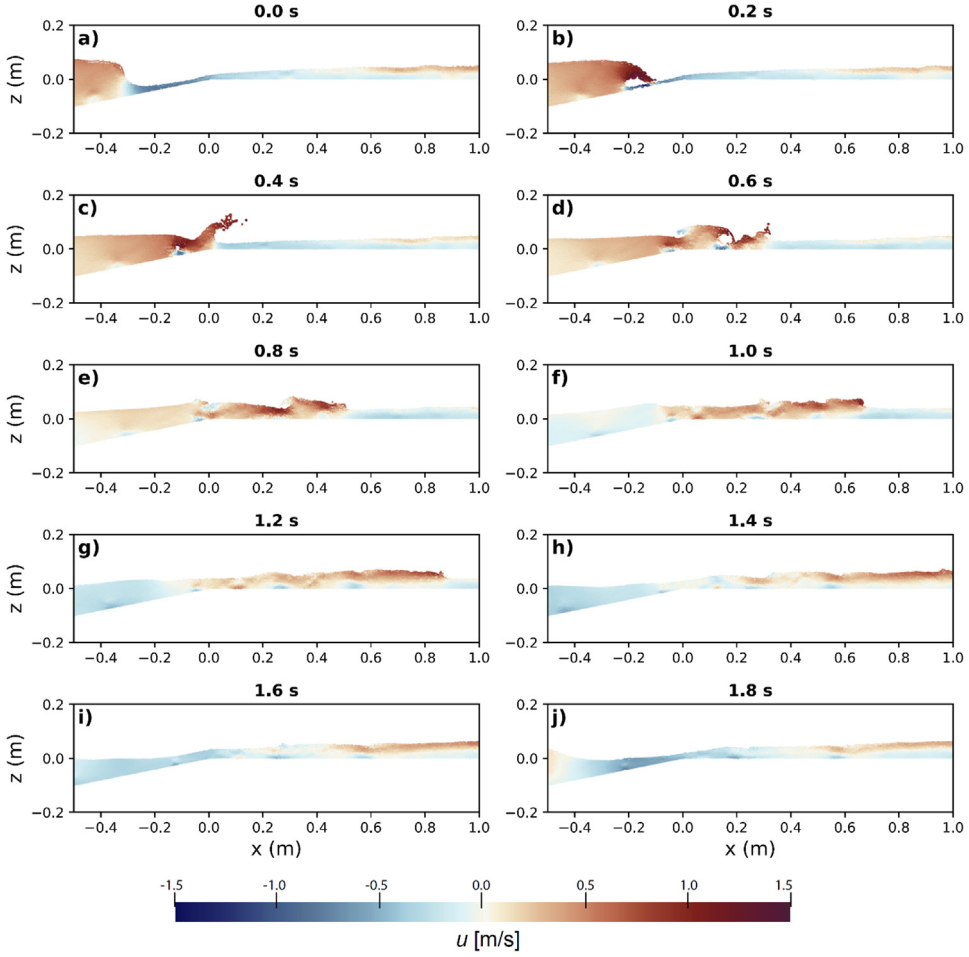

Fig. 3. Example of a breaking wave near the reef crest at ($x = 0$ m) with colours denoting the horizontal (u) component of the velocity field. The output is displayed at 0.2 s interval, where time $t = 0$ s is arbitrarily assigned to the first figure in the sequence.

well predicted (Fig. 6b), reproducing the growth observed on the fore reef, the abrupt decrease in height near the breakpoint, and the near constant values ($H_{rms,IG-H} \approx 1$ cm) across the reef flat. The variation in the low-frequency component of the IG waves ($H_{rms,IG-L}$) across the reef is also generally reproduced accurately by the model, predicting the increase in height shoreward of the reef crest and the oscillation in height, with $H_{rms,IG-L}$ varying from ≈0.5 to 1 cm across the reef flat (Fig. 6c). Only the abrupt changes in $H_{rms,IG-L}$ near the crest are not well-reproduced by the model.

The growth of IG wave heights on the reef causes a substantial increase in the spectral period ($T_{m-1,0}$) shoreward of the reef crest, including an oscillation in $T_{m-1,0}$ due to the varying contribution of the low-frequency IG component, which is accurately predicted by the model (Fig. 6d). The growth in spectral width (ν) is also accurately reproduced, with the model only slightly over-predicting ν at the seaward limit of the reef flat (x = 0–3 m) (Fig. 6e). The mean water level response to the breaking waves (wave setup) closely follows the observations, with $\overline{\eta}$ plateauing to a value of 1.7 cm over the reef flat (Fig. 6f).

As the waves transform across the reef, the shapes (skewness and asymmetry properties) of individual waves change substantially. The waves are initially symmetric ($Sk \approx 0$, $As \approx 0$) on the fore reef but develop positive *Sk* (narrower crests, wider troughs) and negative *As* (steeper faces) as the reef crest is approached (Fig. 7a). The growth of negative *As* develops slightly earlier on the fore reef ($x \approx -1.5$ m), whereas the positive *Sk* develops near the reef crest ($x \approx 0$ m). Eventually on the reef flat ($x > 3$ m) the *Sk* and *As* become relatively constant, decreasing only very slowly (towards zero) across the reef.

Table 1
Comparison between the observed and predicted contributions of wave runup. R_{sig} denotes the significant runup defined in Eq. (10) that is decomposed into setup (R_{setup}) and swash (R_{swash}) contributions. The swash component is further decomposed into sea-swell ($R_{swash,SS}$), high infragravity ($R_{swash,IG-H}$), and low infragravity ($R_{swash,IG-L}$) contributions.

	R_{sig} [m]	$\frac{R_{setup}}{R_{sig}}$	$\frac{R_{swash}}{R_{sig}}$	$\frac{R_{swash,SS}}{R_{swash}}$	$\frac{R_{swash,IG-H}}{R_{swash}}$	$\frac{R_{swash,IG-L}}{R_{swash}}$
Observed	0.033	42%	58%	29%	34%	37%
Predicted	0.032	39%	61%	29%	33%	38%

The model reproduces the spatial evolution of *Sk* and *As* observed across the reef very well.

The detailed spectral evolution of waves across the reef is also accurately predicted, where there is a change from a dominance of energy in SS frequencies on the fore reef ($x < 0$, Fig. 8a–d), a bimodal distribution of energy between SS and IG frequencies within the inner surf zone shoreward of the crest (Fig. 8e), and a gradual shifting to a dominance of IG wave energy towards the back of the reef flat (Fig. 8f–h). Wave runup predictions also agree well with the runup gauge measurements, reproducing the range of low- and high-frequency water level contributions to runup at the shoreline (Fig. 9a). Consistent with the wave spectra at the back of the reef, the runup spectra are dominated by the low-frequency component of IG motions, which is accurately predicted by the model (Fig. 9b). When computing the significant runup (R_{sig}) using Eq. (10), both the observed and predicted values of R_{sig} are in excellent agreement (Table 1). The model also accurately reproduces the proportion of setup and swash contributions

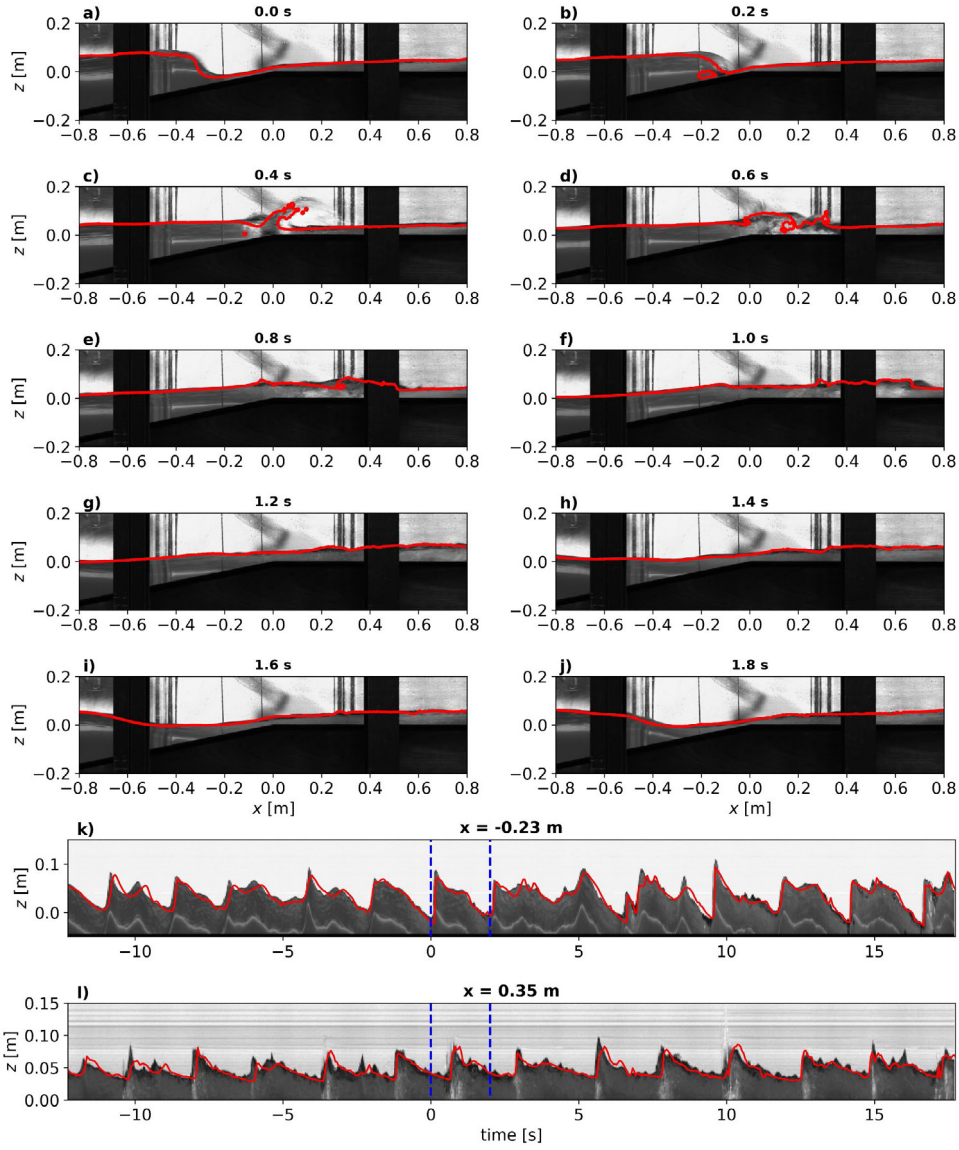

Fig. 4. Comparison of the predicted surface elevation with synchronised georeferenced imagery centred at the reef crest ($x = 0$ m). (a)–(j) Sequence of images at 0.2 s interval with the predicted surface elevation profile superimposed. The image sequence extends over an ~2 s time frame (approximately one peak wave period), focusing on the interval denoted by the vertical blue dashed lines in (k) and (l). (k) Image time stacks (timeseries of vertical pixel columns) over a 30 s period, compared with the predicted surface elevation (solid red line) at $x = -0.23$ m and (l) at $x = 0.35$ m. Note that $t = 0$ s corresponds to the first image in the sequence shown in (a)

to R_{sig} (~40% and 60%, respectively) as well as the *SS*, *IG-H*, and *IG-L* contributions to swash (~30%, ~30%, and ~40%, respectively) (Table 1).

4.2. Wave velocities and directionally-separated wave properties

To decompose incoming and outgoing wave motions using directional separation, velocity timeseries predicted by the model were first compared at the five current metre locations within the model domain (Fig. 10). At all sites, the velocity timeseries were accurately simulated (Fig. 10), and trends in the velocity skewness and asymmetry across the reef were also reproduced (Fig. 7b). While the predictions of the velocity skewness closely matched the observations, there was some discrepancy in the predictions of the velocity asymmetry at the two most seaward locations on the reef flat (Fig. 7b).

The co-located synchronised velocity and water level timeseries were used to directionally-separate the incoming and outgoing (reflected) wave signals (see Sections 3.2 and 3.3), which was applied to both the experimental and model results. For the SS waves, the height of the incoming waves closely follows total $H_{rms,SS}$ due the minimal height of outgoing SS waves (Fig. 11a). On the fore reef, the height of the incoming high-frequency IG waves ($H_{rms,IG-H}$) is smaller than the outgoing waves (Fig. 11b). The incoming signal would be due to incident bound long waves (Longuet-Higgins and Stewart, 1962), and with the reflected heights being larger implies either the surf zone generation of IG waves and/or any reflected IG waves from the reef and beach propagating offshore from the reef (e.g., Pomeroy et al., 2012). The directionally-separated low-frequency IG wave heights $H_{rms,IG-L}$ follow similar trends, with the incoming heights smaller than the outgoing heights on the fore reef, but with incoming heights becoming larger than outgoing heights on the reef flat ($x > 0$ m) (Fig. 11c). Unlike for the outgoing $H_{rms,IG-H}$, which becomes higher on the fore reef relative to the reef flat, the outgoing $H_{rms,IG-L}$ is much more constant across both the fore reef and reef flat. By converting these wave heights to a ratio of outgoing to incoming components, we obtain an estimate of the local reflection coefficient $R = H^{-}_{rms}/H^{+}_{rms}$, where the superscripts '-' and '+' denote the outgoing and incoming components, respectively. Reflection coefficients are weak for the SS waves ($R < 0.3$)

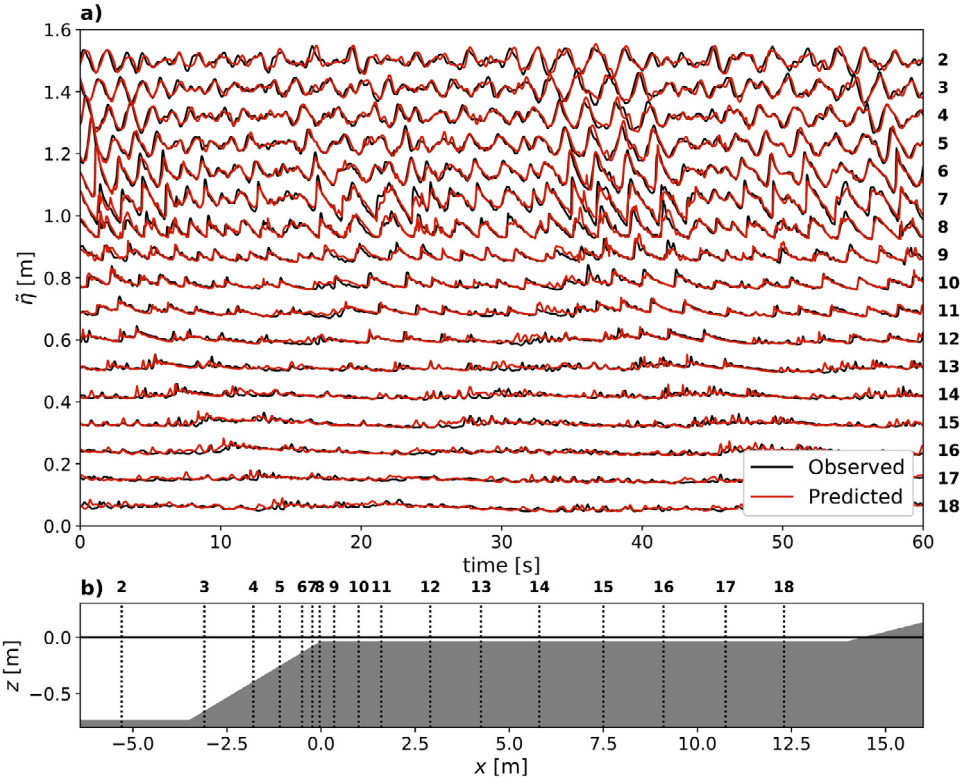

Fig. 5. (a) Comparison of the observed and predicted water levels for a 60 s portion of the timeseries at the wave gauge locations (number to the right), plotted on the same figure with an elevation offset of 7 cm applied incrementally between gauges to avoid overlapping time series. (b) Bathymetry profile with numbered wave gauge locations denoted by the vertical dotted lines. Note that the vertical axis scale has been exaggerated.

across the entire domain, but much larger ($R = 0.5$–2.5) for the two IG components (Fig. 11d). On the reef flat, R varies between 0.5–0.7 for the high IG waves and is larger ($R = 0.7$–1.0) for the low IG waves. On the fore reef, R values for the IG waves reach much higher values (up to 2.5), consistent with the surf zone generation of outgoing IG waves and/or strong reflection from the reef and beach. While there are only five points of comparison where both co-located wave and velocity measurements could be used for directional separation, the agreement between the predicted and observed separated wave heights is generally good. There is generally very good agreement at the three locations on the reef flat ($x > 0$), but R values for the high-frequency IG components are slightly underpredicted at the fore reef location, although similarly high values of $R > 1.5$ are captured.

4.3. Low-frequency wave dynamics

Given the importance of the IG wave contributions to the water level variability over the reef flat, further aspects of IG wave dynamics are compared with the model predictions. Focusing on the IG frequency range ($f < 0.22$ Hz), the spectral distribution of wave energy across the reef shows spatial patterns with bands of high and low energy that are accurately reproduced by the model (Fig. 12). These bands are formed by standing wave motions across the reef flat generated by interactions between incoming and outgoing IG waves, which create a pattern of nodes (locations of low potential energy) and anti-nodes (locations of high potential energy) (Buckley et al., 2018). Based on linear wave theory, at a given cross-shore location (x) the frequencies f_{node} where these nodes should occur can be theoretically predicted as (Buckley et al., 2018)

$$f_{node} = \frac{1}{4}(2n-1)\left(\int_{x}^{x_{shoreline}} \frac{1}{\sqrt{g\left(h+\overline{\eta}\right)}}dx\right)^{-1} \tag{11}$$

where $x_{shoreline}$ is the location of the shoreline and n is the standing wave mode number ($n = 0, 1, 2, \ldots$). The theoretical frequencies of these nodes predicted using Eq. (11) as a function of distance x across the reef flat (red lines, Fig. 12) agree well with the nodes that are present in both the observations and model predictions. This confirms that the IG wave energy on the reef flat is connected to standing wave motions linked to the reef bathymetry profile, with these dynamics well-reproduced by the model.

The forcing of infragravity waves in the nearshore is typically due to breaking wave groups (Longuet-Higgins and Stewart, 1962; Battjes et al., 2004)), including over reef bathymetry profiles (Pomeroy et al., 2012; Péquignet et al., 2009; Becker et al., 2016). Buckley et al. (2018) used the same experimental data to show how the groupiness of the incident SS waves generates IG wave motions in the surf zone that become standing waves over the reef flat that are amplified at the natural frequencies associated with the reef bathymetry profile. To assess the ability of the model to predict the links between incident wave groups and IG wave generation, Fig. 13 shows cross-correlations between the offshore SS wave envelope ($SS_{env,0}$) and the low-pass filtered IG water level signal η_{IG} (see Section 3.3) at locations across the reef. Note that for the model comparison, the $SS_{env,0}$ was referenced to the SWASH water level timeseries at the offshore location ($x = -15.3$ m); however, the η_{IG} timeseries was based on the SWASH results for locations offshore of the model coupling point ($x < -5.5$ m) and based on DualSPHysics results shoreward of this point (Fig. 13b). Both the experimental observations and model predictions show very consistent patterns. Offshore of the reef crest ($x < 0$ m), the correlation between $SS_{env,0}$ and η_{IG} is initially negative, consistent with the presence of incident bound waves (~180 deg out of phase) that propagate at the group velocity (red dashed lines, Fig. 13). Shoreward of the reef crest ($x > 0$ m) the sign of the correlation switches to positive, consistent with the generation of free IG waves via the breakpoint forcing mechanism and shoaling wave groups (Symonds et al., 1982;

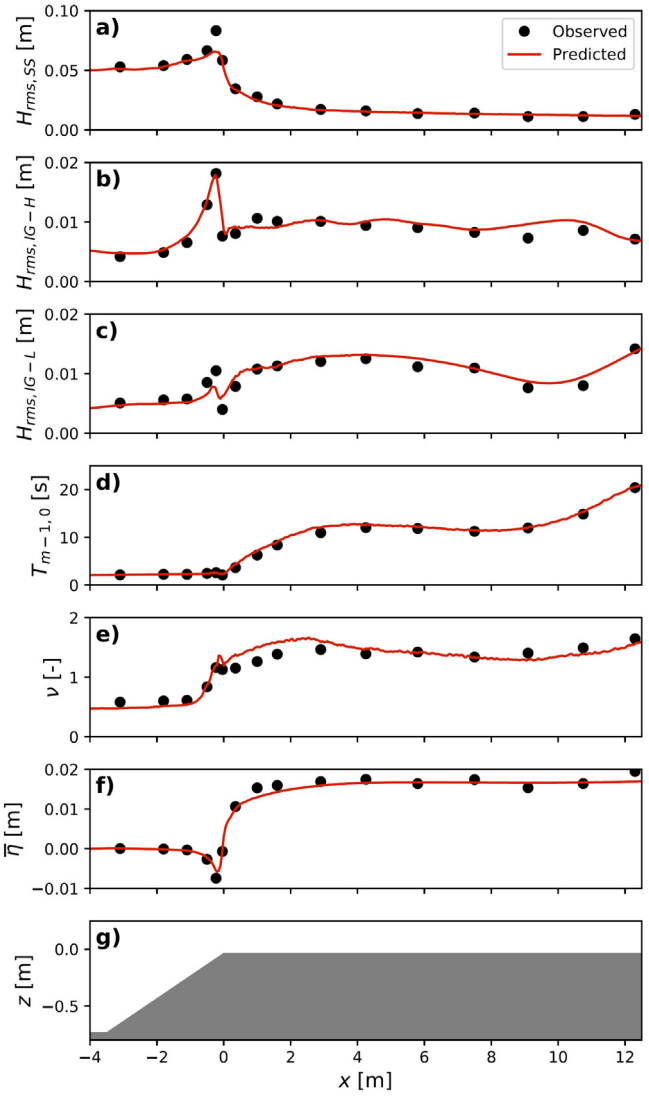

Fig. 6. Bulk wave parameters across the reef, with the observations (black dots) compared against predicted values (red solid line). (a) Sea-swell root-mean-squared wave height ($H_{\mathrm{rms,SS}}$), (b) high infragravity root-mean-squared wave height ($H_{\mathrm{rms,IG-H}}$), (c) low infragravity root-mean-squared wave height ($H_{\mathrm{rms,IG-L}}$), (d) spectral period ($T_{\mathrm{m-1,0}}$), (e) spectral bandwidth (ν), (f) wave setup, and (g) reef bathymetry profile. Note that the vertical axis scale in (g) has been exaggerated.

Pomeroy et al., 2012; Contardo et al., 2021) that propagate shoreward at the shallow water free wave speed (black dashed lines, Fig. 13). Also, consistent with these infragravity wave generation mechanisms, a negative correlation propagates seaward away from the surf zone, which travels at the shallow water wave speed. At the shoreline, the positive correlation returns seaward, consistent with reflection of the incoming free IG waves generated at the crest. There is also evidence of some of this outgoing IG wave energy continuing to propagate offshore past the reef crest onto the fore reef, although the correlation is much weaker than on the reef flat. Overall, these results confirm that the model can accurately reproduce the main features of IG waves across the reef (from generation to propagation). Moreover, the excellent continuity in correlations across the boundary between the DualSPHysics and SWASH models (Fig. 13b), indicates the model coupling approach provides a robust means to efficiently simulate both the irregular wave and associated IG wave dynamics.

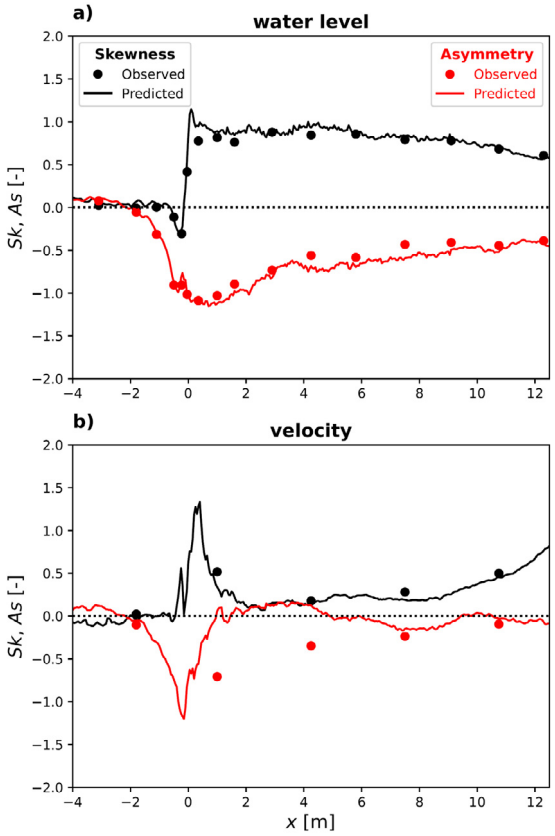

Fig. 7. Comparison of the observed and predicted wave skewness and asymmetry across the reef, computed using Eq. (9) and calculated from the timeseries of (a) water level and (b) velocity.

4.4. Mean currents

The detailed model output is used to investigate the mean current structure, focusing on the region surrounding the reef crest (-2 m $< x <$ $+5$ m) where wave transformation predominantly occurs. In Buckley et al. (2015), the limited point measurements of velocities during the experiment did not make it possible to investigate the detailed vertically-varying mean current fields generated over the reef (e.g., undertow structure), although these data can still provide useful points of comparison with the model predictions in the present study. The modelled mean current field reveals a well-defined undertow flow structure across the reef flat (negative horizontal u velocities) and a complex circulation pattern near the reef crest and along the fore reef slope (Fig. 14b). For reference, the mean water level elevation (solid grey line) and representative crest and trough elevations, defined based on the root-mean-squared wave amplitude ($\pm H_{rms}/2$) (grey dashed lines), are also superimposed. The strength of the undertow decreases with distance across the reef flat ($x > 0$ m), with these cross-shore gradients in horizontal mass fluxes compensated by downward velocities that are strongest near the trough. As the crest and trough elevations are defined here based on H_{rms}, there is some onshore mass flux above the crest elevation due to the mass flux associated with the largest individual waves, which is most pronounced near the crest. There is also a highly-concentrated region of strong flow down the fore reef slope ($x < 0$ m) and strong upwelling occurring further above the slope; this flow pattern leads to a clockwise eddy on the fore reef slope adjacent to the crest. While on the reef flat the interface between onshore and offshore flow ($u = 0$ m s^{-1} white region) coincides approximately with the trough elevation, on the fore reef there is a substantial amount of onshore flow that occurs below the trough.

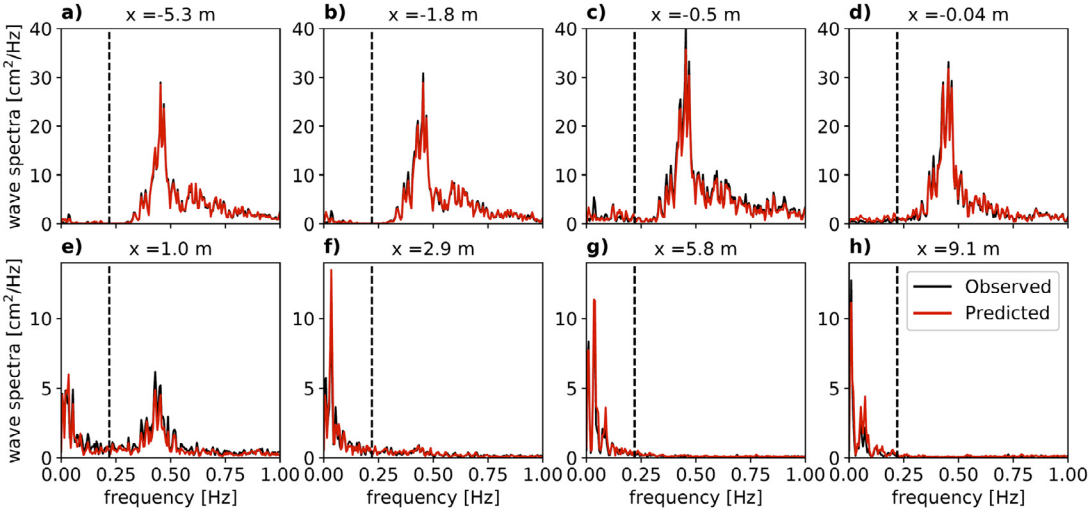

Fig. 8. Evolution of the wave spectra at 8 sites across the reef. Note that the vertical dashed line denotes the frequency cutoff $f_{SS} = 0.22$ Hz that separates sea-swell and infragravity wave frequencies.

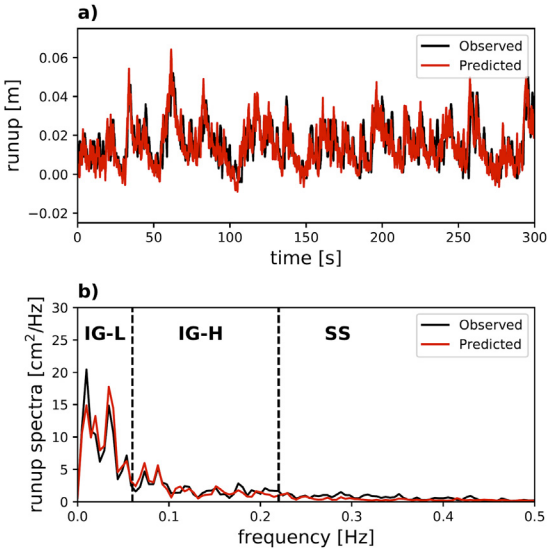

Fig. 9. Wave runup comparison. (a) Example 300 s timeseries comparison of observed versus predicted runup. (b) Runup spectra, with the vertical dashed lines separating sea-swell (SS), high infragravity (IG-H) and low infragravity (IG-L) frequencies.

Despite the limited point measurements of velocities available for comparison, the modelled mean current velocities show consistency with the experimental observations, with negative (seaward-directed) mean currents at these locations that is characteristic of the undertow in the lower part of the water column (Fig. 14c–e). The modelled undertow velocities generally agree well with the experimental measurements at these specific elevations, although the modelled mean velocities are slightly stronger than the observations at the site on the fore reef slope ($x = -1.8$ m) and at the most shoreward site ($x = +4.25$ m) on the reef flat.

5. Discussion

5.1. Model performance

In this study we conducted a comprehensive investigation of the ability of the mesh-free SPH approach, based on DualSPHysics, to accurately simulate the broad range of hydrodynamic processes across a fringing reef profile based on the experimental study by Buckley et al. (2015). This application posed several challenges, notably the need to resolve the dynamics of the violently plunging waves while also requiring running long duration irregular wave simulations that have generally not been considered in analogous CFD models due to the prohibitive computational expense. We demonstrated that the model was able to accurately predict the wide range of these complex hydrodynamic processes, but only with new features recently implemented in DualSPHysics, including the improved model coupling with the nonhydrostatic model SWASH and using recent numerical improvements (i.e., improved fluid–solid boundary conditions and density diffusion terms) that greatly reduced unphysical numerical dissipation (see Appendix A.1).

In the Buckley et al. (2015) experimental setup, a substantial portion of the length of the occupied region of the flume (~30%) contained the shallow 14-m-wide reef flat, which when converted to prototype (field) scale represented a 500 m reef flat that is typical of fringing coral reefs worldwide. With the irregular wave breaking on the reef generating both substantial wave setup (~2 cm) and IG wave motions (~2 cm height for the combined high and low IG contributions), this represents a large portion of the initial still water depth (~4 cm) over the reef flat. To supply this elevated water on the reef flat, a substantial volume of water in the flume offshore of the reef must be transported onto the reef flat leading to a fall in the offshore water level, i.e., any increase in the average water level over the reef will lead to a proportional (~30% in this case) decrease in the average offshore water level per mass conservation. For the case of steady wave setup, water can be added to the flume to compensate this effect of setup and maintain a desired offshore water level. However, for IG wave motions (especially lower frequency contributions that can uniformly raise/lower the entire water level over the reef), this effect is unavoidable and can only be minimised by having a large volume of water offshore of the reef. In the physical modelling experiment, due to the height of these low IG waves being <1 cm (Fig. 6c), the offshore water level would vary at most by <3 mm at these low frequencies, and hence is very small. In the numerical model, directly simulating the large offshore region spanning the complete flume would come at substantial computational expense, which is especially undesirable considering that negligible wave transformation that occurs in this deep region. To improve computational efficiency, the offshore model domain can be truncated. For example, in the present study where the deep region offshore of the reef crest was shortened from 31 m to only 5.5 m, the number of particles simulated decreases by a factor of ~8, which implies a minimum eight-fold increase in computational efficiency assuming approximate linear

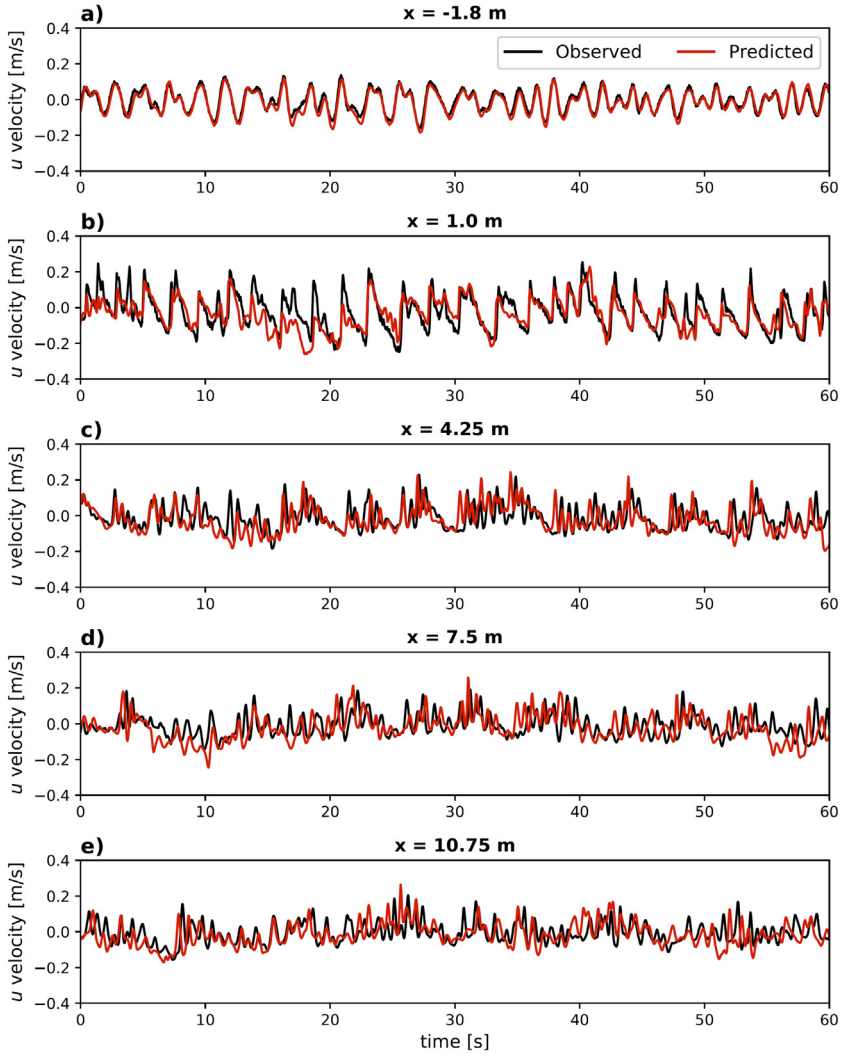

Fig. 10. Comparison of the velocity timeseries (illustrative 60 s period shown) between observations and predictions at 5 locations in the model domain where velocity measurements were available.

scaling with particle number. Yet this shorter offshore domain contains a much smaller volume of water that can substantially amplify offshore water levels as water flows on and off the reef flat. Therefore, while it is possible to directly force this truncated domain at the offshore boundary using a numerical wavemaker or by coupling with the more efficient phase-resolving model SWASH using the multi-layered wavemaker or relaxation zone approach in DualSPHysics (Altomare et al., 2015b, 2018), the constrained volume of water created by any impermeable offshore boundary condition is highly problematic. Instead, in the present study we use new developments in model coupling using an inlet–outlet approach in DualSPHysics (Verbrugghe et al., 2019b), which enabled the volume of water in the SPH domain to dynamically adjust in response to water levels and velocities imposed by large-scale (whole flume) simulations conducted using SWASH. Our results indicate that this coupling approach is both accurate and robust, enabling computationally efficient long duration simulations to be conducted at a fine resolution (dp=3 mm). Such a fine resolution was necessary to accurately reproduce the hydrodynamic processes over the reef flat (see Appendix A.1). With the total H_{rms} averaging ~2.5 cm on the reef flat, the wave height to particle spacing ratio is equivalent to $H_{rms}/dp \sim 8$, which is comparable to the ratio of ~10 that Roselli et al. (2018) recommended for wave propagation problems.

Once waves rapidly transform in the surf zone near the reef crest, the smaller residual waves that propagate across the shallow and wide reef flat can be sensitive to the cumulative effects of any numerical dissipation within the simulations. For this reef profile, initial model testing using the conventional numerical schemes for modelling fluid–solid boundary interactions and density diffusion to reduce noise in DualSPHysics (schemes also widely used in other SPH codes) performed poorly for this application, leading to large discrepancies in wave heights, setup and runup over the reef (see Appendix A.1.2). Using the new modified Dynamic Boundary Condition (mDBC) formulation of English et al. (2021) resulted in much better agreement in wave height and wave runup predictions and some slight improvement in wave setup (see Appendix A.1.2, Table A.4). Wave runup predictions were, in particular, grossly in error using the original DBC, with the swash contribution to runup nearly completely attenuated at the shoreline (see Appendix A.1.2, Fig. A.3) due to the combination of excessive numerical dissipation occurring as waves propagate across the shallow reef flat and as they interact within the swash zone along the beach slope. Within the initial testing, it was also apparent that use of a conventional artificial viscosity formulation with a typical artificial viscosity (α) value of order 0.01 was far too dissipative for simulating waves over this reef profile, despite similar α values having been found to be optimal in many prior WCSPH wave studies (e.g., Altomare et al., 2015a; Roselli et al., 2018; De Padova et al., 2014). The use of an artificial viscosity in WCSPH simulations aims to not only parameterise the effect of physical (combined bulk and shear) viscosity but also to suppress noise arising from pressure / density fluctuations inherent to WCSPH. Test simulations conducted with low viscosity necessary to

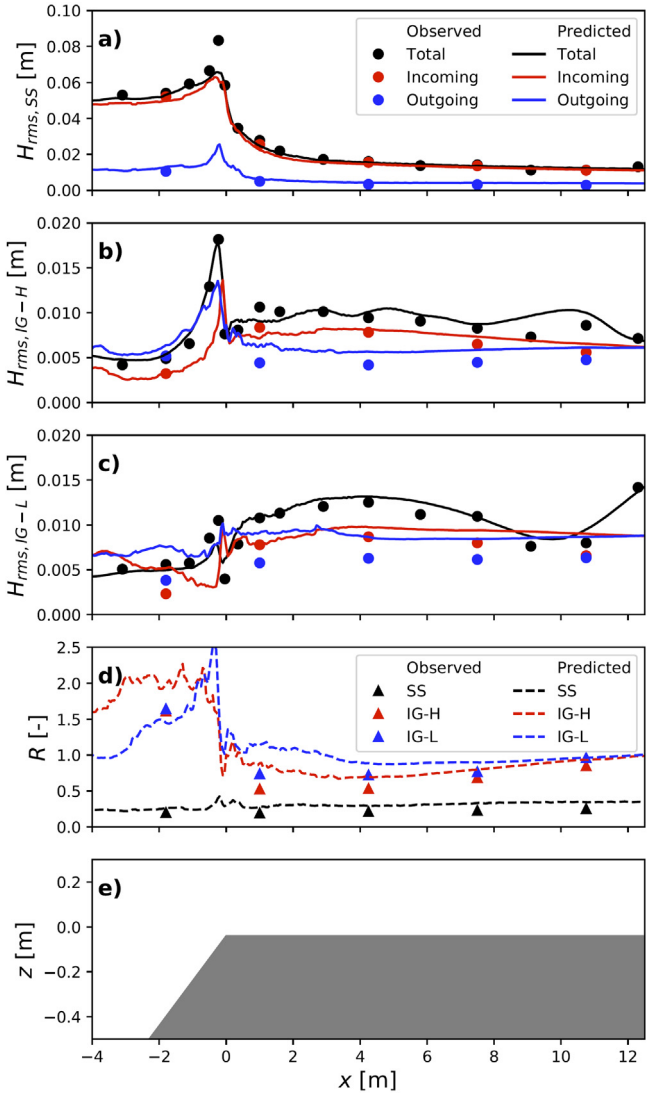

Fig. 11. Comparison between the observed and predicted directionally-separated (a) sea-swell wave height ($H_{\mathrm{rms,SS}}$), (b) high frequency infragravity wave height ($H_{\mathrm{rms,IG-H}}$), and (c) low frequency infragravity wave height ($H_{\mathrm{rms,IG-L}}$). (d) Reflection coefficient R (ratio of reflected and incoming wave heights) for each frequency band. (e) Reef bathymetry profile. Note that the vertical axis scale in (e) has been exaggerated.

reduce numerical wave dissipation across the reef (both using the artificial viscosity and Laminar+SPS schemes) were unstable, necessitating the use of a Density Diffusion Term (DDT) in the simulations. Yet using the original DDT based on Molteni and Colagrossi (2009) generated anomalous mean water levels in regions where wave breaking occurred (see Appendix A.1.2, Figure A3b), which is a known problem when applying this scheme to free surface problems (Antuono et al., 2010). However, using the new DDT scheme of Fourtakas et al. (2019) eliminated this issue, resulting in accurate reproduction of the setup profile across the reef.

It is also noteworthy that the SPH approach was able to accurately reproduce these complex hydrodynamic processes driven by plunging waves using essentially no tuning of model parameters. The choice of parameters that gave optimum performance were all at default or typical values recommended in the literature, including those found optimum in Lowe et al. (2019) for very different wave breaking conditions, including for spilling waves breaking on a mild-sloping beach. However, one important difference in the present simulations from those of Lowe et al. (2019) was the use of low viscosity, due to how effective the new DDT was at suppressing noise in the absence of higher viscosity. In the present study, a Laminar + SPS viscosity formulation was applied using a physically-based kinematic viscosity of $\nu_0 = 1\times10^{-6}$ m^2 s for water, which accurately reproduced both the wave transformation and runup. However, we also obtained comparable (albeit slightly less) accurate results using an artificial viscosity formulation with very low viscosity values (i.e., $\alpha < 10^{-4}$), much lower than typical values of α of order 10^{-2} common in the literature. These results are broadly consistent with the analysis by Meringolo et al. (2019), who showed that due to both the artificial viscosity and DDT having dissipative properties that suppress noise in an WCSPH scheme, when an artificial viscosity is used in the absence of a DDT, an important function of the artificial viscosity is simply noise suppression rather than incorporating the influence of actual physical viscosity. While the present study found that the use of a SPS turbulence model with a physically-based kinematic viscosity performed well for this specific application, as for the case of LES applications on fixed grids, the use of SPS in 2DV cannot strictly resolve the range of turbulent motions that would be present, including correctly resolving the turbulence energy cascade to fine scales that would require resolving 3D turbulent eddies. To be able to properly assess an optimum approach to model turbulent viscosities would require direct measurements of the turbulent fields that were not available in Buckley et al. (2015), as well as comparing simulations conducted in 3D that would be considerably more computationally expensive.

5.2. Reef surf zone processes

Detailed experimental observations of the fine-scale hydrodynamic processes within the roller region of depth-limited breaking waves are still relatively limited, with most of these studies tending to either miss a portion of data within the important crest-to-trough region inside the surf zone (e.g., from optical interference due to aeration) or have used conditions with mild breaking (spilling) conditions where a greater portion of the water column can be robustly sampled (e.g., Govender et al., 2004; Stive and Wind, 1982; Huang et al., 2009; Kimmoun and Branger, 2007; Ting and Kirby, 1994; Stansby and Feng, 2005). For the extreme plunging waves on the steep reef slope in the Buckley et al. (2015) study, where individual waves break on an effectively dry bed and the plunging jets tend to splash up well above incident crest heights (Fig. 4), no analogous fine-scale hydrodynamic observations exist within such breaking waves, which may prove nearly impossible to achieve even using the most advanced experimental techniques presently available. With these highly-resolved SPH simulations proving to be capable of very accurately reproducing the range of hydrodynamic processes that could be measured in Buckley et al. (2015), the use of the detailed model output provides a unique opportunity to fill these observational knowledge gaps.

While several studies have applied phase-resolving Boussinesq and nonhydrostatic models to investigate wave transformation across reefs (e.g., Lashley et al., 2018; Ma et al., 2014; Nwogu and Demirbilek, 2010; Lashley et al., 2020; Rijnsdorp et al., 2021), some studies have highlighted limitations with not directly resolving the vertical structure of overturning breaking waves within such models. For example, in simulations of the same Buckley et al. (2015) experiments using the depth-averaged nonhydrostatic model XBeach-NH, Lashley et al. (2018) found that the model substantially underpredicted both wave setdown and setup. This finding is broadly similar to other studies that have applied phase-resolving depth-averaged nonhydrostatic and Boussinesq models to steeply-sloping bathymetry profiles, where both setdown and setup were also underpredicted (e.g., Skotner and Apelt, 1999; Yao et al., 2012; Liu et al., 2021). However, we also note that da Silva et al. (2021) recently applied the multi-layered nonhydrostatic model SWASH to this same Buckley et al. (2015) experimental case using two vertical layers and found both setdown and setup were better predicted than in Lashley et al. (2018); although still not predicted as accurately

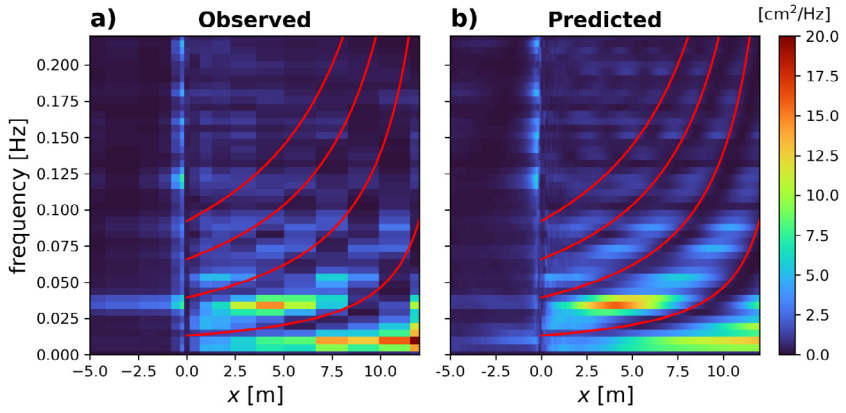

Fig. 12. Spatial variation of the power spectral density of water level (colours in units of $cm^2\ Hz^{-1}$) across the model domain, comparing (a) observations and (b) model predictions. The frequencies focus on the infragravity band ($f < 0.22$ Hz). Red lines denote curves of the theoretical standing wave locations predicted using Eq. (11).

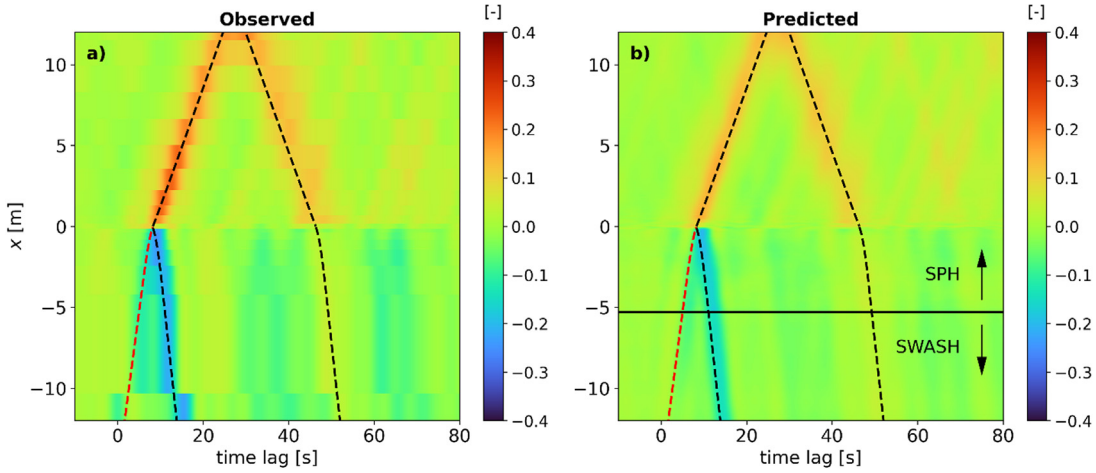

Fig. 13. Cross-correlation of the offshore sea-swell wave envelope (SS_{env0}) with the low-pass filtered ($f < 0.22$ Hz) water level η_{IG} across the domain, comparing the (a) observations and (b) model predictions. Note that the solid horizontal black line in (b) denotes the SWASH-SPH inlet–outlet coupling location ($x = -5.3$ m), with SWASH results shown offshore and SPH results onshore of this point. Red dashed lines denote propagation predicted based on the group velocity using linear wave theory. Black dashed lines denote the propagation predicted based on the shallow water wave speed from linear wave theory.

as in the present study. By analysing the experimental data, Buckley et al. (2015) compared setup predictions from radiation stress gradients estimated from linear wave theory where potential and kinetic energy are in balance, finding that setdown / setup were likewise substantially underpredicted. Instead, they hypothesised that the dynamics within the wave roller were shifting radiation stress gradients shoreward into shallower water; however, given that the experimental observations of Buckley et al. (2015) were limited primarily to wave gauge observations (with only limited near-bed point velocities measurements), most terms in the mean momentum balances could not be calculated to directly verify this. Further work is needed to quantify these mean momentum balances to assess how they can be most robustly captured in phase-resolving (e.g., Boussinesq and nonhydrostatic) wave models, including the relative importance of incorporating both vertical resolution (e.g., as in multi-layered nonhydrostatic models) and/or directly simulating the overturning free surface (e.g., as in detailed CFD models).

While wave setup made a substantial contribution to wave runup in this study, contributing ~40% to significant runup, infragravity wave motions also had a comparably large influence on runup, accounting for ~75% of the significant swash contribution to runup (equivalent to ~45% of the total significant wave runup that includes setup). Sea-swell contributions to wave runup for this reef case were small, accounting for 25% of the swash contribution to runup (equivalent to only 15% of the total significant runup). This dominant contribution of wave setup and IG waves to wave runup is consistent with many prior observations over fringing reef bathymetry profiles (e.g., Cheriton et al., 2016; Shimozono et al., 2015; Nwogu and Demirbilek, 2010). For this particular experimental case, Buckley et al. (2018) showed that the high frequency ($0.22\ \text{Hz} > f \geq 0.06$ Hz) portion of the IG wave spectrum was forced at time scales of the incident wave group forcing; whereas the low-frequency portion ($f < 0.06$ Hz) was resonantly amplified at the natural frequencies of the reef (Eq. (11)), especially for Modes 0 and 1 (Fig. 12). The SPH model simulations were able to correctly reproduce these broad range of wave motions over the reef, including rates of energy conversion and dissipation, that were responsible for the swash contribution to wave runup over this reef profile.

6. Conclusions

In this study, we demonstrated the capability of the mesh-free SPH modelling approach, based on DualSPHysics, to predict the complicated hydrodynamic processes generated by plunging irregular waves over a fringing reef by simulating the physical modelling study of Buckley et al. (2015). The bathymetry profile, consisting of a steeply-sloping fore reef slope where waves violently break, followed by a wide and shallow reef flat where organised wave motions reform and propagate

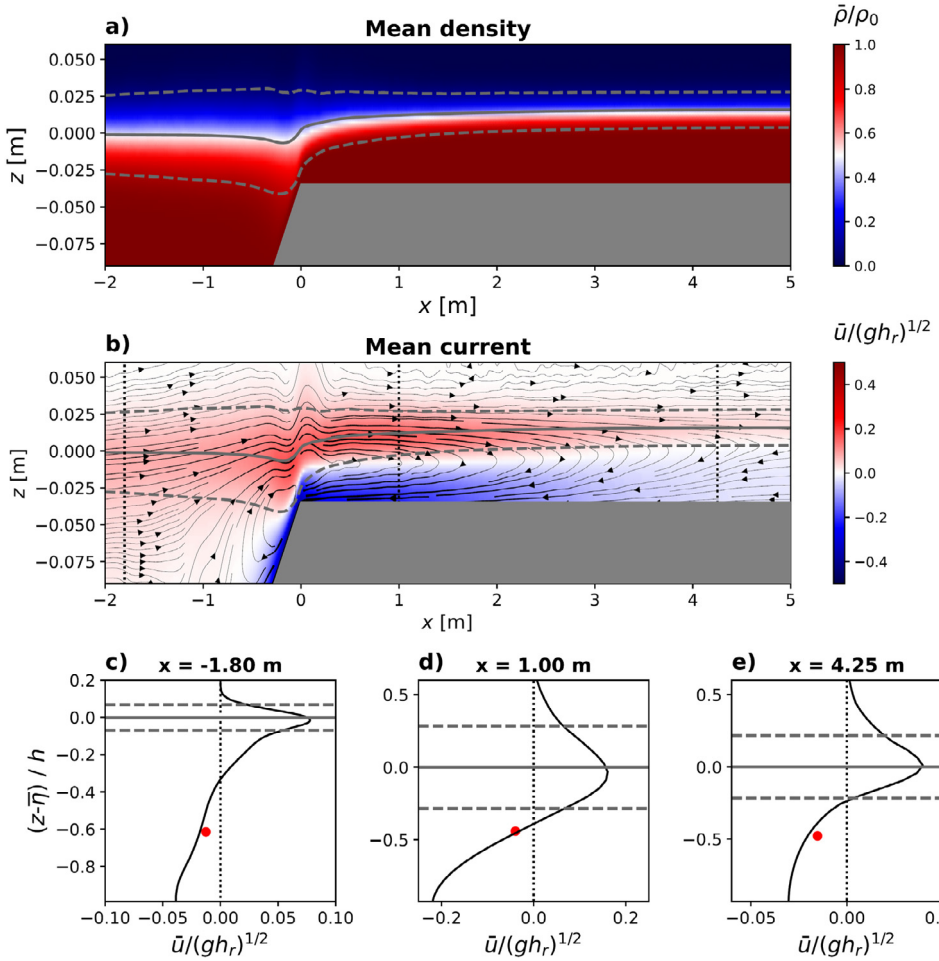

Fig. 14. (a) Time-averaged density field $\bar{\rho}$ normalised by the reference density ρ_0=1000 kg m^{-3}. (b) Horizontal component of the mean current velocity ($\bar{u}$) normalised by the linear shallow water wave speed $(gh_r)^{1/2}$ over the reef flat. In (a) and (b), the solid grey line denotes the mean water level profile and the two grey dashed lines denote the range of the root-mean-squared wave height (i.e., defining a representative crest-to-trough region of the waves). In (b) the vertical dotted lines denote locations where single point velocity measurement data were collected. (c)–(e) Comparison of the normalised horizontal mean current profiles with the point velocity measurements (red dots) at the three locations in (b). Note that the solid grey horizontal line denotes the elevation of the mean water level ($z = \bar{\eta}$) and the horizontal dashed lines denote the representative crest and trough elevations.

to the shoreline, can create a number of challenges for numerical models, in general. While the WCSPH approach used in this study has previously proven to be well-suited for simulating nearshore wave breaking processes, the numerics can have dissipative characteristics that can pose problems for applications where inviscid flow features must be accurately modelled; for example, applications where non-breaking waves propagate over relatively long distances (Dalrymple and Rogers, 2006). Results from this study show that conventional approaches to describe fluid–solid boundary interactions (i.e., based on the standard DBC approach) and common techniques used to suppress noise in pressure fields in the WCSPH method (i.e., by using elevated artificial viscosities or applying a DDT based on the conventional δ-SPH approach) were far too dissipative and/or inaccurate to resolve the evolution of waves across the wide and shallow reef flat. However, using a new modified DBC approach based on English et al. (2021) and a new DDT based on Fourtakas et al. (2019), dissipation and noise was able to be suppressed while using lower (physically-based) viscosity values.

The most obvious drawback of conducting such highly-resolved CFD model simulations, in general, is the required computation expense, which has tended to limit many surf zone applications to simulations of relatively short duration driven by regular waves. However, the present model simulations were greatly accelerated by the efficient parallelisation of the weakly compressible SPH approach on GPUs and by substantially reducing the model domain by robust coupling to the nonhydrostatic wave-flow model SWASH. With this coupled modelling approach, long duration irregular wave simulations were achieved using a single GPU, which were necessary to resolve the critical low-frequency portion of the wave spectrum over the reef that made a major contribution to wave runup at the shoreline.

While conventional phase-averaged (spectral) models and phase-resolving models (e.g., Boussinesq and nonhydrostatic) that empirically parameterise the wave breaking process usually require some prior available experimental data to calibrate and verify model predictions, an apparent advantage of the SPH approach has been the limited need to tune model parameters. This is supported by the fact that the numerical parameters used in this study closely mirrored those used in Lowe et al. (2019) that considered very different breaking wave conditions, including spilling waves on a mild-sloping plane beach. The primary difference in the present study was the use of improved numerical methods in DualSPHysics (i.e., the new mDBC and DDT) that reflect improvements designed to reduce numerical dissipation within the weakly-compressible SPH approach. While the mesh-free SPH approach was successfully demonstrated in this study, we must acknowledge that the application of mesh-based CFD models to this case at similarly high resolution could prove to be equally capable of

Table A.1
Model performance quantified using the normalised root mean squared error between the observations and predictions ($NRMSE_{expt}$) for different values of the smoothing coefficient (*coefh*). Note that the * denotes the default *coefh* = 1.5 value used within the simulation reported in the main text.

coefh [–]	$NRMSE_{expt}$		
	Wave height	Setup	Runup
1.2	0.078	0.083	0.043
1.4	0.065	0.049	0.038
1.5*	0.065	0.048	0.035
1.6	0.066	0.049	0.043
1.8	0.062	0.050	0.038

performing well; such an assessment would require a comprehensive study comparing mesh-based CFD model results (e.g., from RANS-based models) directly to these present SPH simulations.

Finally, while the focus of this present study was on investigating the surf zone hydrodynamic processes over an idealised bathymetry profile, there would likely be numerous other advantages with the mesh-free SPH approach when attempting to simulate more complex geometries (including bathymetric / topographic features and coastal structures) that would likely confer some advantages over mesh-based CFD models that may not naturally conform to fixed grids. The SPH approach is continuously proving its strength at simulating the hydrodynamics in a range of coastal applications, including flows through complex porous structures, fluid–structure interactions with deformable objects, and floating body problems that are ideally-suited to the mesh-free approach (Gotoh and Khayyer, 2018; Lind et al., 2020; Domínguez et al., 2021). Due to the weakly-compressible SPH method being readily parallelisable, including running efficiently on GPUs that possess greater computing power relative to CPUs, both larger-scale and longer duration applications will be increasingly feasible as computational resources continuously advance. This will enable a number of new coastal problems to be simulated that have historically proven too computationally expensive for CFD model applications.

CRediT authorship contribution statement

R.J. Lowe: Conceptualisation, Methodology, Software, Validation, Formal analysis, Investigation, Writing – original draft, Writing – review & editing, Visualisation, Project administration. **C. Altomare:** Conceptualisation, Methodology, Software, Validation, Investigation, Writing – review & editing. **M.L. Buckley:** Conceptualisation, Methodology, Software, Formal analysis, Investigation, Writing – review & editing. **R.F. da Silva:** Software, Investigation, Writing – review & editing. **J.E. Hansen:** Writing – review & editing. **D.P. Rijnsdorp:** Writing – review & editing. **J.M. Domínguez:** Software, Writing – review & editing. **A.J.C. Crespo:** Writing – review & editing.

Declaration of competing interest

The authors declare the following financial interests/personal relationships which may be considered as potential competing interests: Ryan Lowe reports financial support and administrative support were provided by The University of Western Australia. Ryan Lowe reports financial support was provided by Australian Research Council.

Acknowledgements

This work was supported by resources provided by the Pawsey Supercomputing Centre with funding from the Australian Government and the Government of Western Australia. We thank Tomo Suzuki and Ben Rogers for insightful discussions that helped improve the study at different stages. This work was supported by funding from an Australian Research Council Discovery Project grant (DP200101545). The development of the DualSPHysics code was partially financed by Xunta de Galicia, Spain, Consellería de Cultura, Spain, Educación e Universidade, Spain, under project ED431C 2021/44 "Programa de Consolidación e Estructuración de Unidades de Investigación Competitivas". We thank Falk Feddersen and two anonymous reviewers for valuable comments that helped to improve the manuscript. Any use of trade, firm, or product names is for descriptive purposes only and does not imply endorsement by the U.S. Government.

Appendix

A.1. Statistical convergence and model parameter sensitivity

A.1.1. Influence of simulation duration on bulk parameter results

In initial testing, we assessed how the statistical properties of bulk parameters converged with the number N of individual SS waves simulated, where N is defined as the duration of the simulation normalised by the offshore peak wave period T_p (Fig. A.1). The full duration (960 s) simulation described in the main text thus corresponds to resolving $N = 425$ individual SS waves. To assess how the bulk parameter results converged as a function of the number of waves simulated, we computed the root-mean-squared-error (*RMSE*), defined as

$$RMSE = \sqrt{\frac{\sum_{i=1}^{n}\left(X_{compare} - X_{ref}\right)^2}{n}} \tag{A.1}$$

where $X_{compare}$ denotes the variable that is being compared, X_{ref} denotes a reference value that is being compared against, and n denotes the number of data points used in the comparison. Using Eq. (A.1), a normalised root-mean-squared error (*NRMSE*) is then defined as

$$NRMSE = \frac{RMSE}{X_{\text{ref}}^{\max} - X_{\text{ref}}^{\min}} \tag{A.2}$$

where the superscripts 'max' and 'min' denote the maximum and minimum values, respectively. To assess how key bulk wave parameter results converged to the full (960 s) duration results, we computed a normalised root-mean-squared error $NRMSE_{960s}$ by defining X_{ref} in Eqs. (A.1) and (A.2) based on the 960 s results and comparing the results at all n model output locations (Fig. A.1). By comparing results from different simulation durations, we could then evaluate how $NRMSE_{960s}$ varied with the number (N) of SS waves simulated. For the case of wave runup, we also computed an $NRMSE_{960s}$ using the runup spectra by comparing each of the n data points in the spectrum from the full duration simulation to the corresponding points in the spectra at a given simulation duration.

Fig. A.1 shows that the $NRMSE_{960s}$ values for SS wave heights ($H_{rms,SS}$), high frequency IG wave heights ($H_{rms,IG-H}$), and wave setup all converged to approximately the full duration values (i.e., $NRMSE_{960s} < 0.01$) for simulation durations of $N \approx 100 - 120$ waves (equivalent to 220–270 s); whereas the low-frequency IG wave heights ($H_{rms,IG-L}$) took $N \approx 200$ waves (equivalent to 450 s) to converge. The wave runup spectra also took a relatively long time to converge to the full duration results, with $NRMSE_{960s} < 0.01$ occurring only after $N \approx 330$ waves (740 s) were simulated.

A.1.2. Model parameter sensitivity

Several applications of SPH models to simulate waves have investigated the sensitivity of model performance to various parameters, especially: (1) particle resolution, defined by the initial inter-particle distance (*dp*), (2) the smoothing coefficient (*coefh*), and (3) parameters associated with the viscosity formulation (e.g., Roselli et al., 2018; González-Cao et al., 2019; De Padova et al., 2014; Lowe et al., 2019). Here we evaluate how model predictions of the total root-mean squared wave height (H_{rms}), setup ($\overline{\eta}$), and wave runup (η_{runup}) varied in response to these same parameters, as well as some additional parameters related to numerical formulations (namely treatment of solid boundary

Table A.2
Sensitivity analysis and model performance characteristics for simulations with varying initial inter-particle distance (dp), where $H_{rms,0}$ denotes the offshore root-mean-squared wave height. Note that the * denotes the default dp=3 mm value used within the simulation reported in the main text and 'Particles' denotes the initial number of particles in the domain at the start of the simulation.

dp [mm]	$H_{rms,0}/dp$	Particles	Computation time [h]	$NRMSE_{expt}$ [–]		
				Wave height	Setup	Runup
2	25.0	907460	184.7	0.059	0.042	0.081
3*	16.6	418504	72.1	0.064	0.048	0.035
5	10	158106	24.6	0.066	0.046	0.049
7	7.1	87999	13.8	0.087	0.057	0.055
9	5.5	53249	8.0	0.250	0.063	0.058
11	4.5	37909	6.1	0.383	0.080	0.051
14	3.6	25170	4.5	0.644	0.166	0.170

Table A.3
Model performance characteristics for simulations using the artificial viscosity approach with variable values of artificial viscosity (α).

α [–]	$NRMSE_{expt}$		
	Wave height	Setup	Runup
0	0.064	0.048	0.039
10^{-6}	0.064	0.050	0.039
10^{-4}	0.066	0.048	0.048
0.005	0.066	0.045	0.036
0.010	0.065	0.052	0.064
0.015	0.067	0.056	0.074
0.020	0.070	0.060	0.074
0.040	0.073	0.065	0.073

Table A.4
Model performance with the default settings used within the simulation reported in the main text, with the new modified Dynamic Boundary Condition of English et al. (2019) (denoted 'mDBC') and the new Density Diffusion Term (DDT) of Fourtakas et al. (2019), compared against results using the original Dynamic Boundary Condition of Crespo et al. (2007) (denoted 'DBC') and the original DDT of Molteni and Colagrossi (2009).

Scenario	$NRMSE_{expt}$		
	Wave height	Setup	Runup
Default: mDBC, DDT (Fourtakas et al., 2019)	0.065	0.048	0.035
DBC, DDT (Fourtakas et al., 2019)	0.081	0.053	0.176
mDBC, DDT (Molteni and Colagrossi, 2009)	0.053	0.073	0.069

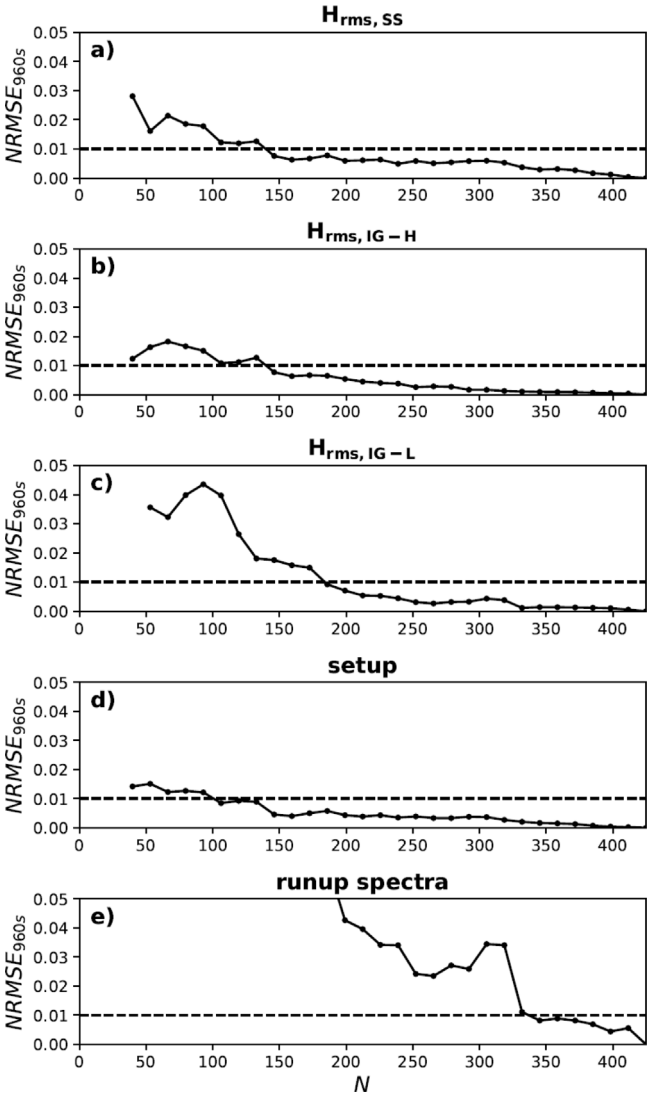

Fig. A.1. Convergence of the bulk wave statistics. (a) Sea-swell root-mean-squared wave height ($H_{rms,SS}$), (b) high frequency infragravity wave height ($H_{rms,IG-H}$), (c) low frequency infragravity wave height ($H_{rms,IG-L}$), (d) wave setup, and (e) the runup spectra, as a function of the simulation duration. The normalised root-mean-squared errors ($NRMSE_{960s}$) are defined with reference to the full duration period of 960 s. Results are expressed as a function of the equivalent number (N) of peak wave periods simulated, based on the simulation time used in the averaging normalised by the peak wave period $T_p = 2.26$ s. The horizontal dashed lines denote the 1% $NRMSE_{960s}$ *value*.

conditions and the density diffusion term in Eq. (4)). Model performance was similarly quantified using a normalised root-mean-squared error ($NRMSE_{\text{expt}}$), referenced to the experimentally-measured by replacing X_{ref} in Eqs. (A.1) and (A.2) with X_{expt}, and here taking N as the number of independent data points being compared. Note that for both wave height and setup, the $NRMSE_{\text{expt}}$ values were computed using the series of H_{rms} and $\overline{\eta}$ values at the $N = 16$ measurement locations within the model domain (i.e., as in Fig. 6); whereas the $NRMSE_{\text{expt}}$ for runup was defined based on comparing the series of frequency bins ($N = 60$) in the runup spectra (i.e., as in Fig. 9b). In addition, to investigate how the model results converged with changes in dp, we also computed a second measure of performance by comparing the results to those obtained at the finest resolution dp=2 mm considered, i.e., by replacing X_{expt} with X_{fine} to calculate $NRMSE_{\text{fine}}$ based on Eqs. (A.1) and (A.2), where the subscript 'fine' denotes the finest resolution results. In this way, the scaling behaviour of model performance with dp becomes independent of any potential errors in the experimental measurements (see Fig. A.2).

For these sensitivity tests, we consider the default case to have the settings used in the final simulation described in the main text (i.e., with dp = 3 mm, *coefh*=1.5 and using the Laminar+SPS viscosity formulation), and then assess how changes in model parameters influence performance. Given the computational demand of the simulations, these sensitivity tests used shorter 300 s simulations (equivalent to $N = 132$ waves), which based on Fig. A.1 was adequate to resolve the spectral wave evolution across the reef (except for a portion of very low-frequency wave energy), the wave setup profile, and a portion of the wave runup spectra.

The results were largely insensitive to variations in the smoothing coefficient (*coefh*) values between 1.4–1.8; only for the smallest value *coefh*=1.2 was there some reduction in the accuracy of the wave height and setup predictions (Table A.1). Thus, for the final simulation, an intermediate value *coefh*=1.5 was used.

The sensitivity tests conducted to investigate the influence of particle distance dp (Table A.2) show that the predictions of wave heights, setup and runup rapidly converge towards the experimental measurements as dp decreases from 14 mm to 5 mm (Fig. A.2); however, there are only small reductions in $NRMSE_{\text{expt}}$ for $dp \leq 5$ mm. To balance model performance with computational efficiency, a dp = 3 mm was used for the final simulation, which reproduced the experimental observations of wave height, setup and runup to within approximately 5% error (Table A.2). To investigate how the results converged based on the

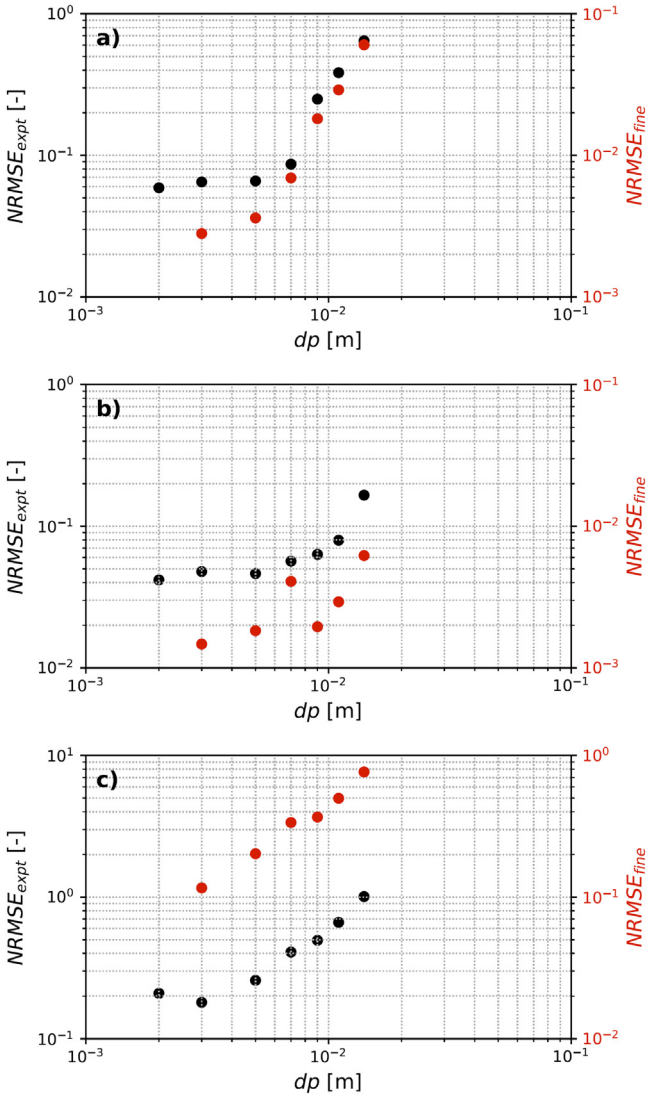

Fig. A.2. (a) Convergence characteristics of the normalised root mean squared error (NRMSE) with varying initial inter-particle spacing (dp) based on comparison of a) wave height distributions (H_{rms}), (b) setup distributions ($\overline{\eta}$), and (c) wave runup (η_{runup}) spectra. NRMSE$_{expt}$ (black dots) and NRMSE$_{fine}$ (red dots) denote the NRMSE calculated using Eq. (A.1) and (A.2) by referencing the model predictions against the experimental data and finest resolution results ($dp = 2$ mm), respectively.

numerical output alone, in Fig. A.2 we also include the response of the $NRMSE_{\text{fine}}$ in which the error is referenced to the finest simulation with ($dp = 2$ mm). While the $NRMSE_{\text{fine}}$ for wave height and runup continues to decrease as dp decreases for all values, $NRMSE_{\text{fine}}$ displays a more complicated pattern for wave setup, initially decreasing as dp is reduced from 14 mm to 9 mm but then showing no consistent improvement for $dp \leq 7$ mm.

While the simulations reported in the main text used the Laminar+SPS viscosity formulation, we also considered the use of a conventional artificial viscosity term that treats the viscous dissipation term in Eq. (5) as

$$\Gamma_i = \Pi_{ij} \nabla_i W_{ij} \tag{A.3}$$

where the artificial viscosity term Π_{ij} is defined as (Monaghan, 1992):

$$\Pi_{ij} = \begin{cases} \frac{-\alpha \overline{c_{ij}} \mu_{ij}}{\overline{\rho_{ij}}} & \vec{u}_{ij} \cdot \vec{r}_{ij} < 0 \\ 0 & \vec{u}_{ij} \cdot \vec{r}_{ij} > 0 \end{cases} \tag{A.4}$$

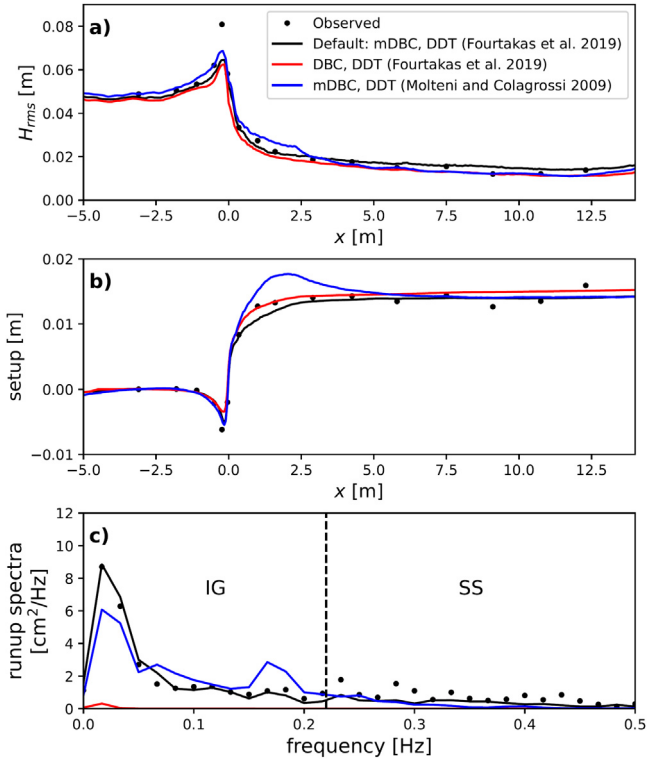

Fig. A.3. Sensitivity of the model performance to bottom boundary condition and density diffusion schemes, comparing the default simulation using both the new modified Dynamic Boundary Condition of English et al. (2019) (denoted 'New mDBC') and the new Density Diffusion Term of Fourtakas et al. (2019) (denoted 'New DDT'), compared against results using the original Dynamic Boundary Condition of Crespo et al. (2007) (denote 'Original DBC') and the original Density Diffusion Term of Molteni and Colagrossi (2009) (denoted 'Original DDT') for a) root-mean-squared wave height (H_{rms}), (b) wave setup, and (c) the wave runup spectra.

with $\mu_{ij} = h_{SPH} \vec{u}_{ij} \cdot \vec{r}_{ij} / \left(\vec{r}_{ij}^2 + \varepsilon^2 \right)$ for $\varepsilon^2 = 0.01 h_{SPH}$, $\overline{c_{ij}} = 0.5 \left(c_i + c_j \right)$ is the mean speed of sound, and α is a coefficient (termed artificial viscosity) that determines the rate of viscous dissipation. In these sensitivity tests, we varied α from a large value ($\alpha = 0.04$) to zero (Table A.3). The results for wave height and setup were not very sensitive to variations in α over this large range but showed some slight reduction in $NRMSE_{\text{expt}}$ at the lower values of α. However, the runup predictions showed more variable performance with α, with lowest $NRMSE_{\text{expt}}$ for $\alpha \leq 0.005$. These results indicate that low to negligible values of artificial viscosity best reproduced the experimental observations, which is different from the surf zone simulations by Lowe et al. (2019) and numerous other wave studies using SPH (e.g., De Padova et al., 2014 that have found optimal performance with α of order 0.01.

Finally, we assessed how the new numerical formulations describing fluid–solid boundary interactions and the density diffusion term affect model performance (Fig. A.3, Table A.4). When using the original Dynamic Boundary Condition (DBC) approach (Crespo et al., 2007), the model performance deteriorates substantially for both wave height and runup. Inspection of the wave height (H_{rms}) profiles in Fig. A.3 indicates that the conventional DBC approach leads to greater dissipation of wave energy across the wide and shallow reef flat, as well as substantial energy loss in the shallow swash flows at the shoreline (not shown), which together substantially reduces wave runup at the shoreline. Likewise, wave height and setup predictions using the new density diffusion term by Fourtakas et al. (2019), were generally much improved compared to results using the original density diffusion term of Molteni and Colagrossi (2009). With the original density diffusion term, there are substantial water level anomalies affecting both H_{rms} and wave setup within the active breaking region of the surf zone.

References

Altomare, C., Crespo, A.J., Domínguez, M., Suzuki, T., 2015a. Applicability of smoothed particle hydrodynamics for estimation of sea wave impact on coastal structures. Coast. Eng. 96, 1–12.

Altomare, C., Domínguez, J.M., Crespo, A., González-Cao, J., Suzuki, T., Gómez-Gesteira, M., Troch, P., 2017. Long-crested wave generation and absorption for SPH-based DualSPHysics model. Coast. Eng. 127, 37–54.

Altomare, C., Domínguez, J., Crespo, A., Suzuki, T., Caceres, I., Gómezgesteira, M., 2015b. Hybridization of the wave propagation model SWASH and the mesh-free particle method SPH for real coastal applications. Coast. Eng. J. 57, 1550024-1-1550024-34.

Altomare, C., Tagliafierro, B., Dominguez, J.M., Suzuki, T., Viccione, G., 2018. Improved relaxation zone method in SPH-based model for coastal engineering applications. Appl. Ocean Res. 81, 15–33.

Antuono, M., Colagrossi, A., Marrone, S., 2012. Numerical diffusive terms in weakly-compressible SPH schemes. Comput. Phys. Comm. 183, 2570–2580.

Antuono, M., Colagrossi, A., Marrone, S., Molteni, D., 2010. Free-surface flows solved by means of SPH schemes with numerical diffusive terms. Comput. Phys. Comm. 181, 532–549.

Batchelor, G., 1974. An Introduction to Fluid Dynamics. Cambridge University Press.

Battjes, J., Bakkenes, H., Janssen, T., Van Dongeren, A.R., 2004. Shoaling of subharmonic gravity waves. J. Geophys. Res. Oceans 109.

Battjes, J., 1978. Energy loss and set-up due to breaking of random waves. Coast. Eng. 1978.

Becker, J., Merrifield, M., Yoon, H., 2016. Infragravity waves on fringing reefs in the tropical Pacific: Dynamic setup. J. Geophys. Res. Oceans 121, 3010–3028.

Bertin, X., De Bakker, A., Van Dongeren, A., Coco, G., Andre, G., Ardhuin, F., Bonneton, P., Bouchette, F., Castelle, B., Crawford, W.C., 2018. Infragravity waves: From driving mechanisms to impacts. Earth-Sci. Rev. 177, 774–799.

Blenkinsopp, C., Chaplin, J., 2007. Void fraction measurements in breaking waves. Proc. R. Soc. A Math. Phys. Eng. Sci. 463, 3151–3170.

Bruder, B.L., Brodie, K.L., 2020. CIRN Quantitative Coastal imaging toolbox. SoftwareX 12, 100582.

Buckley, M.L., Lowe, R.J., Hansen, J.E., Van Dongeren, A.R., 2015. Dynamics of wave setup over a steeply sloping fringing reef. J. Phys. Oceanogr. 45, 3005–3023.

Buckley, M.L., Lowe, R.J., Hansen, J.E., Van Dongeren, A.R., Storlazzi, C.D., 2018. Mechanisms of wave-driven water level variability on reef-fringed coastlines. J. Geophys. Res. Oceans 123, 3811–3831.

Chella, M.A., Bihs, H., Myrhaug, D., Muskulus, M., 2016. Hydrodynamic characteristics and geometric properties of plunging and spilling breakers over impermeable slopes. Ocean Model. 103, 53–72.

Cheriton, O.M., Storlazzi, C.D., Rosenberger, K.J., 2016. Observations of wave transformation over a fringing coral reef and the importance of low-frequency waves and offshore water levels to runup, overwash, and coastal flooding. J. Geophys. Res. Oceans 121, 3121–3140.

Contardo, S., Lowe, R.J., Hansen, J.E., Rijnsdorp, D.P., Dufois, F., Symonds, G., 2021. Free and forced components of shoaling long waves in the absence of short-wave breaking. J. Phys. Oceanogr. 51, 1465–1487.

Crespo, A.J., Domínguez, J.M., Rogers, B.D., Gómez-Gesteira, M., Longshaw, S., Canelas, R., Vacondio, R., Barreiro, A., García-Feal, O., 2015. DualSPHysics: Open-source parallel CFD solver based on smoothed particle hydrodynamics (SPH). Comput. Phys. Comm. 187, 204–216.

Crespo, A., Gómez-Gesteira, M., Dalrymple, R.A., 2007. Boundary Conditions Generated by Dynamic Particles in SPH Methods, Vol. 5, No. 173. CMC-Tech Science Press.

da Silva, R.F., Rijnsdorp, D.P., Hansen, J.E., Lowe, R., Buckley, M., Zijlema, M., 2021. An efficient method to calculate depth-integrated, phase-averaged momentum balances in non-hydrostatic models. Ocean Model. 165, 101846.

Dalrymple, R.A., Rogers, B., 2006. Numerical modeling of water waves with the SPH method. Coast. Eng. 53, 141–147.

De Padova, D., Dalrymple, R.A., Mossa, M., 2014. Analysis of the artificial viscosity in the smoothed particle hydrodynamics modelling of regular waves. J. Hydraul. Res. 52, 836–848.

Domínguez, J.M., Crespo, A.J., Gómez-Gesteira, M., 2013. Optimization strategies for CPU and GPU implementations of a smoothed particle hydrodynamics method. Comput. Phys. Comm. 184, 617–627.

Domínguez, J.M., Fourtakas, G., Altomare, C., Canelas, R.B., Tafuni, A., García-Feal, O., Martínez-Estévez, I., Mokos, A., Vacondio, R., Crespo, A.J., 2021. DualSPHysics: from fluid dynamics to multiphysics problems. Comput. Part. Mech. 1–29.

English, A., Domínguez, J., Vacondio, R., Crespo, A., Stansby, P., Lind, S., Chiapponi, L., Gómez-Gesteira, M., 2021. Modified dynamic boundary conditions (mDBC) for general-purpose smoothed particle hydrodynamics (SPH): application to tank sloshing, dam break and fish pass problems. Comput. Part. Mech. 1–15.

English, A., Domínguez, J., Vacondio, R., Crespo, A., Stansby, P., Lind, S., Gómez-Gesteira, M., 2019. Correction for dynamic boundary conditions. In: Proceedings of the 14th International SPHERIC Workshop. Exeter, UK. pp. 25–27.

Falter, J.L., Lowe, R.J., Zhang, Z., Mcculloch, M., 2013. Physical and biological controls on the carbonate chemistry of coral reef waters: effects of metabolism, wave forcing, sea level, and geomorphology. PLoS One 8, e53303.

Fourtakas, G., Dominguez, J.M., Vacondio, R., Rogers, B.D., 2019. Local uniform stencil (LUST) boundary condition for arbitrary 3-D boundaries in parallel smoothed particle hydrodynamics (SPH) models. Comput. & Fluids 190, 346–361.

Gawehn, M., Van Dongeren, A., Van Rooijen, A., Storlazzi, C.D., Cheriton, O.M., Reniers, A., 2016. Identification and classification of very low frequency waves on a coral reef flat. J. Geophys. Res. Oceans 121, 7560–7574.

González-Cao, J., Altomare, C., Crespo, A., Domínguez, J., Gómez-Gesteira, M., Kisacik, D., 2019. On the accuracy of DualSPHysics to assess violent collisions with coastal structures. Comput. & Fluids 179, 604–612.

Gotoh, H., Khayyer, A., 2018. On the state-of-the-art of particle methods for coastal and ocean engineering. Coast. Eng. J. 60, 79–103.

Gotoh, H., Shao, S., Memita, T., 2004. SPH-LES model for numerical investigation of wave interaction with partially immersed breakwater. Coast. Eng. J. 46, 39–63.

Govender, K., Mocke, G., Alport, M., 2004. Dissipation of isotropic turbulence and length-scale measurements through the wave roller in laboratory spilling waves. J. Geophys. Res. Oceans 109.

Higuera, P., Lara, J.L., Losada, I.J., 2013. Simulating coastal engineering processes with OpenFOAM®. Coast. Eng. 71, 119–134.

Hirt, C.W., Nichols, B.D., 1981. Volume of fluid (VOF) method for the dynamics of free boundaries. J. Comput. Phys. 39, 201–225.

Hofland, X., Altomare, C., Oosterlo, P., 2017. Prediction formula for the spectral wave period Tm-1, 0 on mildly sloping shallow foreshores. Coast. Eng. 123, 21–28.

Huang, Z.-C., Hsiao, S.-C., Hwung, H.-H., Chang, K.-A., 2009. Turbulence and energy dissipations of surf-zone spilling breakers. Coast. Eng. 56, 733–746.

Jacobsen, N.G., Fuhrman, D.R., Fredsøe, J., 2012. A wave generation toolbox for the open-source CFD library: OpenFoam®. Internat. J. Numer. Methods Fluids 70, 1073–1088.

Janssen, T., Battjes, J., Van Dongeren, A., 2003. Long waves induced by short-wave groups over a sloping bottom. J. Geophys. Res. Oceans 108.

Kimmoun, O., Branger, H., 2007. A particle image velocimetry investigation on laboratory surf-zone breaking waves over a sloping beach. J. Fluid Mech. 588 (353).

Lashley, C.H., Roelvink, D., Van Dongeren, A., Buckley, M.L., Lowe, R.J., 2018. Nonhydrostatic and surfbeat model predictions of extreme wave run-up in fringing reef environments. Coast. Eng. 137, 11–27.

Lashley, C.H., Zanuttigh, B., Bricker, J.D., Van Der Meer, J., Altomare, C., Suzuki, T., Roeber, V., Oosterlo, P., 2020. Benchmarking of numerical models for wave overtopping at dikes with shallow mildly sloping foreshores: Accuracy versus speed. Environ. Model. Softw. 130, 104740.

Lind, S.J., Rogers, B.D., Stansby, P.K., 2020. Review of smoothed particle hydrodynamics: towards converged Lagrangian flow modelling. Proc. R. Soc. Lond. Ser. A Math. Phys. Eng. Sci. 476, 20190801.

Liu, Y., Li, S., Liao, Z., Liu, K., 2021. Physical and numerical modeling of random wave transformation and overtopping on reef topography. Ocean Eng. 220, 108390.

Lo, E.Y., Shao, S., 2002. Simulation of near-shore solitary wave mechanics by an incompressible SPH method. Appl. Ocean Res. 24, 275–286.

Longuet-Higgins, M.S., Stewart, R., 1962. Radiation stress and mass transport in gravity waves, with application to 'surf beats'. J. Fluid Mech. 13, 481–504.

Lorensen, W.E., Cline, H.E., 1987. Marching cubes: A high resolution 3D surface construction algorithm. ACM Siggraph Comput. Graph. 21, 163–169.

Lowe, R.J., Buckley, M.L., Altomare, C., Rijnsdorp, D.P., Yao, Y., Suzuki, T., Bricker, J., 2019. Numerical simulations of surf zone wave dynamics using Smoothed Particle Hydrodynamics. Ocean Model. 144, 101481.

Ma, G., Shi, F., Kirby, J.T., 2012. Shock-capturing non-hydrostatic model for fully dispersive surface wave processes. Ocean Model. 43-44, 22–35.

Ma, G., Su, S.-F., Liu, S., Chu, J.-C., 2014. Numerical simulation of infragravity waves in fringing reefs using a shock-capturing non-hydrostatic model. Ocean Eng. 85, 54–64.

Madsen, P.A., Sørensen, O.R., Schäffer, H.A., 1997. Surf zone dynamics simulated by a Boussinesq type model. Part I. Model description and cross-shore motion of regular waves. Coast. Eng. 32, 255–287.

Makris, C.V., Memos, C.D., Krestenitis, Y.N., 2016. Numerical modeling of surf zone dynamics under weakly plunging breakers with SPH method. Ocean Model. 98, 12–35.

Meringolo, D.D., Marrone, S., Colagrossi, A., Liu, Y., 2019. A dynamic δ-SPH model: How to get rid of diffusive parameter tuning. Comput. & Fluids 179, 334–355.

Molteni, D., Colagrossi, A., 2009. A simple procedure to improve the pressure evaluation in hydrodynamic context using the SPH. Comput. Phys. Comm. 180, 861–872.

Monaghan, J.J., 1992. Smoothed particle hydrodynamics. Annu. Rev. Astron. Astrophys. 30, 543–574.

Monaghan, J.J., 1994. Simulating free surface flows with SPH. J. Comput. Phys. 110, 399–406.

Mostert, W., Deike, L., 2020. Inertial energy dissipation in shallow-water breaking waves. J. Fluid Mech. 890.

Nwogu, O., Demirbilek, Z., 2010. Infragravity wave motions and runup over shallow fringing reefs. J. Waterw. Port Coast. Ocean Eng. 136, 295–305.

Péquignet, A.C.N., Becker, J.M., Merrifield, M.A., Aucan, J., 2009. Forcing of resonant modes on a fringing reef during tropical storm Man-Yi. Geophys. Res. Lett. 36.

Pomeroy, A., Lowe, R., Symonds, G., Van Dongeren, A., Moore, C., 2012. The dynamics of infragravity wave transformation over a fringing reef. J. Geophys. Res. Oceans 117.

Rijnsdorp, D.P., Buckley, M.L., Da Silva, R.F., Cuttler, M.V., Hansen, J.E., Lowe, R.J., Green, R.H., Storlazzi, C.D., 2021. A numerical study of wave-driven mean flows and setup dynamics at a coral reef-lagoon system. J. Geophys. Res. Oceans 126, e2020JC016811.

Roeber, V., Cheung, K.F., Kobayashi, M.H., 2010. Shock-capturing Boussinesq-type model for nearshore wave processes. Coast. Eng. 57, 407–423.

Roelvink, J., 1993. Dissipation in random wave groups incident on a beach. Coast. Eng. 19, 127–150.

Roenby, J., Bredmose, H., Jasak, H., 2016. A computational method for sharp interface advection. R. Soc. Open Sci. 3, 160405.

Roselli, R.A.R., Vernengo, G., Altomare, C., Brizzolara, S., Bonfiglio, L., Guercio, R., 2018. Ensuring numerical stability of wave propagation by tuning model parameters using genetic algorithms and response surface methods. Environ. Model. Softw. 103, 62–73.

Ruessink, B., Ramaekers, G., Van Rijn, L., 2012. On the parameterization of the free-stream non-linear wave orbital motion in nearshore morphodynamic models. Coast. Eng. 65, 56–63.

Shao, S., Ji, C., 2006. SPH computation of plunging waves using a 2-D sub-particle scale (SPS) turbulence model. Internat. J. Numer. Methods Fluids 51, 913–936.

Shi, F., Kirby, J.T., Harris, J.C., Geiman, J.D., Grilli, S.T., 2012. A high-order adaptive time-stepping TVD solver for Boussinesq modeling of breaking waves and coastal inundation. Ocean Model. 43, 36–51.

Shimozono, T., Tajima, Y., Kennedy, A.B., Nobuoka, H., Sasaki, J., Sato, S., 2015. Combined infragravity wave and sea-swell runup over fringing reefs by super typhoon haiyan. J. Geophys. Res. Oceans 120, 4463–4486.

Skotner, C., Apelt, C.J., 1999. Application of a Boussinesq model for the computation of breaking waves: Part 2: Wave-induced setdown and setup on a submerged coral reef. Ocean Eng. 26, 927–947.

Smagorinsky, J., 1963. General circulation experiments with the primitive equations: I. The basic experiment. Mon. Weather Rev. 91, 99–164.

Sous, D., Tissier, M., Rey, V., Touboul, J., Bouchette, F., Devenon, J.-L., Chevalier, C., Aucan, J., 2019. Wave transformation over a barrier reef. Cont. Shelf Res. 184, 66–80.

Stansby, P.K., Feng, T., 2005. Kinematics and depth-integrated terms in surf zone waves from laboratory measurement. J. Fluid Mech. 529, 279–310.

Stive, M.J., Wind, H.G., 1982. A study of radiation stress and set-up in the nearshore region. Coast. Eng. 6 (1), 1–25, (1982).

Svendsen, I.A., 2006. Introduction to Nearshore Hydrodynamics. World Scientific.

Symonds, G., Huntley, D.A., Bowen, A.J., 1982. Two-dimensional surf beat: Long wave generation by a time-varying breakpoint. J. Geophys. Res. Oceans 87, 492–498.

Tafuni, A., Domínguez, J., Vacondio, R., Crespo, A., 2018. A versatile algorithm for the treatment of open boundary conditions in smoothed particle hydrodynamics GPU models. Comput. Methods Appl. Mech. Engrg. 342, 604–624.

Taylor, P.A., Miller, J.C., 2012. Measuring the effects of artificial viscosity in SPH simulations of rotating fluid flows. Mon. Not. R. Astron. Soc. 426, 1687–1700.

Thornton, E.B., Guza, R., 1983. Transformation of wave height distribution. J. Geophys. Res. Oceans 88, 5925–5938.

Ting, F.C., Kirby, J.T., 1994. Observation of undertow and turbulence in a laboratory surf zone. Coast. Eng. 24, 51–80.

Ting, F.C., Kirby, J.T., 1996. Dynamics of surf-zone turbulence in a spilling breaker. Coast. Eng. 27, 131–160.

Ting, J.T., 1995. Dynamics of surf-zone turbulence in a strong plunging breaker. Coast. Eng. 24, 177–204.

Tissier, M., Dekkers, J., Reniers, A., Pearson, S., Van Dongeren, A., 2018. Undular bore development over a laboratory fringing reef. Coast. Eng. Proc. 5, 3–53.

Torres-Freyermuth, A., Lara, J.L., Losada, I.J., 2010. Numerical modelling of short-and long-wave transformation on a barred beach. Coast. Eng. 57, 317–330.

Vacondio, R., Altomare, C., De Leffe, M., Hu, X., Le Touzé, D., Lind, S., Marongiu, J.-C., Marrone, S., Rogers, B.D., Souto-Iglesias, A., 2021. Grand challenges for Smoothed Particle Hydrodynamics numerical schemes. Comput. Part. Mech. 8, 575–588.

Verbrugghe, T., Domínguez, J., Altomare, C., Tafuni, A., Vacondio, R., Troch, P., Kortenhaus, A., 2019a. Non-linear wave generation and absorption using open boundaries within DualSPHysics. Comput. Phys. Comm.

Verbrugghe, T., Stratigaki, V., Altomare, C., Domínguez, J.M., Troch, P., Kortenhaus, A., 2019b. Implementation of open boundaries within a two-way coupled SPH model to simulate nonlinear wave–structure interactions. Energies 12 (697), https://doi.org/10.3390/en12040697.

Violeau, D., 2012. Fluid Mechanics and the SPH Method: Theory and Applications. Oxford University Press.

Violeau, D., Rogers, B.D., 2016. Smoothed particle hydrodynamics (SPH) for free-surface flows: past, present and future. J. Hydraul. Res. 54, 1–26.

Wen, H., Ren, B., 2018. A non-reflective spectral wave maker for SPH modeling of nonlinear wave motion. Wave Motion 79, 112–128.

Wendland, H., 1995. Piecewise polynomial, positive definite and compactly supported radial functions of minimal degree. Adv. Comput. Math. 4, 389–396.

Yao, Y., Huang, Z., Monismith, S.G., Lo, E.Y., 2012. 1DH Boussinesq modeling of wave transformation over fringing reefs. Ocean Eng. 47, 30–42.

Zijlema, M., Stelling, G., Smit, P., 2011. SWASH: An operational public domain code for simulating wave fields and rapidly varied flows in coastal waters. Coast. Eng. 58, 992–1012.